Moist versus Dry Baroclinic Instability in a Simplified Two-Layer Atmospheric Model with Condensation and Latent Heat Release

Julien Lambaerts, Guillaume Lapeyre, Vladimir Zeitlin

Moist versus Dry Baroclinic Instability in a Simplified Two-Layer Atmospheric Model with Condensation and Latent Heat Release

JULIEN LAMBAERTS, GUILLAUME LAPEYRE, AND VLADIMIR ZEITLIN

Laboratoire de Météorologie Dynamique, Ecole Normale Supérieure/CNRS/Universtité Pierre et Marie Curie/IUF, Paris, France

(Manuscript received 28 July 2011, in final form 27 October 2011)

ABSTRACT

The authors undertake a detailed analysis of the influence of water vapor condensation and latent heat release upon the evolution of the baroclinic instability. The framework consists in a two-layer rotating shallow-water model with moisture coupled to dynamics through mass exchange between the layers due to condensation/precipitation. The model gives all known in literature models of this kind as specific limits. It is fully nonlinear and ageostrophic. The reference state is a baroclinic Bickley jet. The authors first study its ''dry'' linear instability and then use the most unstable mode to initialize high-resolution numerical simulations of the life cycle of the instability in nonprecipitating (moisture being a passive tracer) and precipitating cases. A new-generation well-balanced finite-volume scheme is used in these simulations.

The evolution in the nonprecipitating case follows the standard cyclonic wave-breaking life cycle of the baroclinic instability, which is reproduced with a high fidelity. In the precipitating case, the onset of condensation significantly increases the growth rate of the baroclinic instability at the initial stages due to production of available potential energy by the latent heat release. Condensation occurs in frontal regions and wraps up around the cyclone, which is consistent with the moist cyclogenesis theory and observations. Condensation induces a clear-cut cyclone–anticyclone asymmetry. The authors explain the underlying mechanism and show how it modifies the equilibration of the flow at the late stages of the saturation of the instability. In spite of significant differences in the evolution, only weak differences in various norms of the perturbations remain between precipitating and nonprecipitating cases at the end of the saturation process.

1. Introduction

Baroclinic instability of the large-scale tropospheric jet has been invoked to explain the growth of midlatitude synoptic systems since the pioneering studies of Charney (1947), Eady (1949), and Phillips (1954). Its mechanism is now well understood, as well as its nonlinear saturation, so-called baroclinic life cycles (e.g., Pedlosky 1979). Being a large-scale phenomenon, baroclinic instability is traditionally analyzed within the quasigeostrophic (QG) approximation. Yet, the ageostrophic aspects such as surface frontogenesis (Hoskins and West 1979) need also to be taken into account. An often-missing factor in the studies of baroclinic instability is moisture, although the evolution of synoptic perturbations is accompanied by typical large-scale condensation patterns (Bluestein 1993).

Because of complexity of the thermodynamics of the moist air (Emanuel 1994) subject to phase transitions, one usually seeks to parameterize the condensation of the water vapor and the associated latent heat release at synoptic scales. Most of the parameterizations trigger condensation once the moisture content exceeds a threshold value depending on saturation and convective available potential energy (CAPE) such as the Betts–Miller scheme (Betts and Miller 1986), which corresponds to the convective quasi-equilibrium approximation (e.g., Arakawa and Schubert 1974; Emanuel et al. 1994). This parameterization expresses precipitation and related latent heat release in terms of relaxation of specific humidity toward an equilibrium profile. The threshold effect introduced in this way is essentially nonlinear and forbids linearization of the system equations. Consequently, the standard method of linear stability analysis and modal decomposition cannot be applied. Even if a piecewise linearization can be performed (inside each precipitating or nonprecipitating region), the resulting modes would strongly depend on the initial partition of the domain. The

Corresponding author address: Vladimir Zeitlin, LMD-ENS, 24 rue Lhomond, 75005 Paris, France.
E-mail: zeitlin@lmd.ens.fr

DOI: 10.1175/JAS-D-11-0205.1

fully nonlinear (Lyapunov) stability analysis is thus necessary. This intrinsic difficulty explains a lack of understanding of the moist baroclinic instability. In general, moisture is supposed to essentially reduce the static stability of the flow (e.g., Emanuel et al. 1987; Lapeyre and Held 2004; O'Gorman 2011). A large part of the studies of moist instability deal with the convective instability of second kind (CISK) type of instability, which appears when the condensation heating is directly related to the low-level convergence of moisture (Charney and Eliassen 1964; Lindzen 1974). The earlier theoretical studies on moist baroclinic instability treated the linear stability of an unstable jet in simple quasigeostrophic models using CISK parameterization (Shukla 1978; Mak 1982; Bannon 1986). They took into account neither the threshold effect, assuming a perpetually saturated domain, nor the evolution of humidity. Emanuel et al. (1987) accomplished this type of analysis using a parameterization assuming neutrality in ascents with respect to slantwise moist convection. This could be done by adequately separating the domain into dry (descending) and moist (ascending) air regions. All of these studies indicate the increase of the growth rate of the instability due to the condensation and latent heat release. Nonlinear numerical simulations were performed both with quasigeostrophic (Emanuel et al. 1987) and primitive equations (Gutowski et al. 1992; Whitaker and Davis 1994; Balasubramanian and Yau 1994, 1996; Balasubramanian and Garner 1997) showing that during the evolution of baroclinic instability the lower-level cyclones were intensified by moist processes. Such cyclone/anticyclone asymmetry was highlighted in the analysis of the influence of moisture on turbulent baroclinic eddies in a quasigeostrophic model (Lapeyre and Held 2004). This influence was also studied in hurricane formation from turbulence (Schecter and Dunkerton 2009; Schecter 2011).

In the present paper, we analyze in detail the influence of water vapor condensation and latent heat release on the development of baroclinic instability in the framework of a Phillips-like simplified layered model that facilitates both conceptual understanding and high-resolution numerical simulations. We use a moist-convective two-layer rotating shallow-water (mc2RSW) model recently developed and tested in Lambaerts et al. (2011b). It represents the atmosphere as a moist lower layer and a dry upper layer with mass and momentum exchanges due to moist convection. Layered atmospheric models of this type with moist physics were previously considered in the literature: Gill (1982) and Frierson et al. (2004) worked with the linear baroclinic rotating shallow-water (RSW)-type of model, Lapeyre and Held (2004) studied a quasigeostrophic model, and Bouchut et al. (2009) studied the one-layer mcRSW model. We should stress that all of these previously considered models can be derived from the mc2RSW model in specific limits (Lambaerts et al. 2011b). The mc2RSW model is fully nonlinear, takes into account the ageostrophic motions, and couples the moisture evolution with dynamics via condensation and latent heat release. A robust finite-volume numerical scheme (Bouchut and Zeitlin 2010), which conserves steady states in geostrophic balance (''well-balanced scheme'') is available for the model.

We follow the same strategy as Lambaerts et al. (2011a), who studied the influence of moisture on barotropic instability: after performing a detailed linear stability analysis of the dry basic configuration, we extract the most unstable mode and initialize the direct numerical simulations of nonlinear saturation with this mode. We perform parallel numerical simulations, with the condensation switched off and on. Comparison of these simulations allows us to highlight new processes associated with latent heat release, which have a crucial influence upon the moist baroclinic instability and life cycles of atmospheric perturbations.

The paper is organized as follows: In section 2, we present the mc2RSW model. The background jet configuration and the linear stability analysis of a uniform subsaturated state with no condensation and thus no influence of the moisture field upon other fields are presented in section 3. The numerical setup for the simulations is described in section 4. The dry simulation with no condensation is then compared in detail to the moist, or precipitating, one, where precipitation is triggered beyond the saturation threshold. The initial stages of the development of instability are analyzed in section 5, whereas its nonlinear saturation is studied in section 6. Summary and discussion are presented in section 7. Appendixes contain the details of the linear stability analysis, a discussion of the readjustment of the basic flow due to the discretization errors, and a discussion of the dependence of the obtained results on the parameters of the model, respectively.

2. mc2RSW model

We use a simplified two-layer model of the atmosphere derived in Lambaerts et al. (2011b). It results from the vertical averaging of the dry primitive equations in pseudoheight coordinates (Hoskins and Bretherton 1972), by considering a rigid upper surface, a constant geopotential at the lower free surface, and constant potential temperature θ in each layer. The resulting equations are completed by the one for the vertically integrated specific humidity $Q = \int q\, dz$, which is supposed to be present in the lower layer only. The humidity equation includes a precipitation sink P. Moist convection is

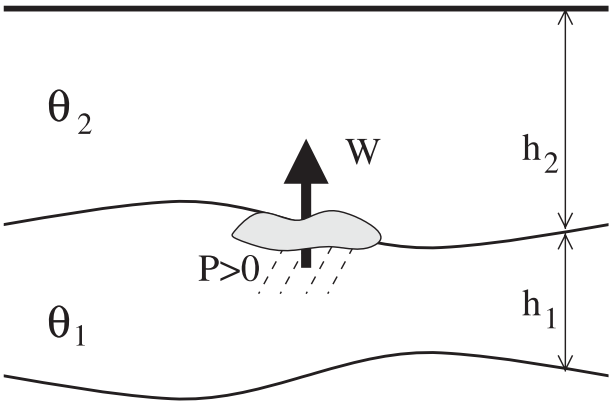

FIG. 1. Sketch of the mc2RSW model.

introduced with the help of an extra vertical velocity W across the interface between the two layers. As shown in Lambaerts et al. (2011b), it can be related to condensation by using the conservation of the moist enthalpy $\theta + Lq/c_p$, where L is the latent heat release coefficient and c_p is the specific heat. A sketch of the model is presented in Fig. 1. More details can be found in Lambaerts et al. (2011b).

The equations of mc2RSW model are as follows:

$$\partial_t \boldsymbol{v}_1 + (\boldsymbol{v}_1 \cdot \nabla)\boldsymbol{v}_1 + f\mathbf{k}\times\boldsymbol{v}_1 = -g\nabla(h_1 + h_2), \quad (2.1)$$

$$\partial_t \boldsymbol{v}_2 + (\boldsymbol{v}_2 \cdot \nabla)\boldsymbol{v}_2 + f\mathbf{k}\times\boldsymbol{v}_2 = -g\nabla(h_1 + \alpha h_2) + \frac{\boldsymbol{v}_1 - \boldsymbol{v}_2}{h_2}\beta P, \quad (2.2)$$

$$\partial_t h_1 + \nabla\cdot(h_1\boldsymbol{v}_1) = -\beta P,$$
$$\partial_t h_2 + \nabla\cdot(h_2\boldsymbol{v}_2) = +\beta P, \quad \text{and} \quad (2.3)$$

$$\partial_t Q + \nabla\cdot(Q\boldsymbol{v}_1) = -P, \quad (2.4)$$

where g is the gravitational acceleration; f is the Coriolis parameter, which is supposed to be constant throughout this paper (f-plane approximation); and $\alpha = \theta_2/\theta_1$ the stratification parameter. The index 1 (2) denotes the lower (upper) layer. Equations (2.1)–(2.3) are the momentum and the mass conservation equations in each layer, and Eq. (2.4) is the moisture conservation. Condensation (or precipitation, because they are synonyms in this idealized model) P appears as a sink in Eq. (2.4), whereas latent heat release corresponds to the convective exchange $W = \beta P$ in Eq. (2.3). This latter also induces a transfer of momentum to the upper layer represented by the last term on the rhs of Eq. (2.2). We use a Betts–Miller-type parameterization for the precipitation,

$$P = \frac{Q - Q^s}{\tau}H(Q - Q^s), \quad (2.5)$$

which brings humidity Q back to the saturation value Q^s (chosen to be constant, for simplicity), with a relaxation time τ. Here, $H(\cdot)$ denotes the Heaviside function. This scheme does not depend on and does not include CAPE and we consider only the layer-integrated moisture No evaporation effects are considered below for simplicity; otherwise, an evaporation source should be added in Eq. (2.4).

Moist enthalpy in the lower layer is defined by $m_1 = h_1 - \beta Q$ and is locally conserved,

$$\partial_t m_1 + \nabla\cdot(m_1\boldsymbol{v}_1) = 0. \quad (2.6)$$

Because the upper layer is dry, the moist enthalpy is not defined there. The evolution of the potential vorticity (PV) in each layer is given by

$$(\partial_t + \boldsymbol{v}_1\cdot\nabla)\frac{\zeta_1 + f}{h_1} = \frac{\zeta_1 + f}{h_1^2}\beta P \quad \text{and} \quad (2.7)$$

$$(\partial_t + \boldsymbol{v}_2\cdot\nabla)\frac{\zeta_2 + f}{h_2} = -\frac{\zeta_2 + f}{h_2^2}\beta P + \frac{\mathbf{k}}{h_2}\cdot\left[\nabla\times\left(\frac{\boldsymbol{v}_1 - \boldsymbol{v}_2}{h_2}\beta P\right)\right], \quad (2.8)$$

where $\zeta_i = \mathbf{k}\cdot(\nabla\times\boldsymbol{v}_i) = \partial_x v_i - \partial_y u_i$ ($i = 1, 2$) is the relative vorticity. Thus, PV is not a Lagrangian invariant in the precipitating regions. Precipitation introduces a source (sink) of PV $(-1)^{i-1}(\zeta_i + f)h_i^{-2}\beta P$ in the lower (upper) layer and an additional source in the upper layer, due to vorticity induced by the moist convection drag [cf. Eq. (2.8)].

3. Linear stability of the baroclinic Bickley jet

Our reference state will be a baroclinic Bickley jet. We first analyze its linear stability using the dry equations (ignoring P and Q). The model then becomes the standard two-layer rotating shallow-water model. The unstable mode found in this analysis will be used to compare the precipitating and nonprecipitating simulations with the same initial conditions.

a. Baroclinic Bickley jet

The basic state is chosen to be a geostrophically balanced zonal jet on the f plane defined by the dimensionless velocity and height profiles,

$$\frac{\overline{\mathbf{v}}_i}{U} = [\overline{u}_i(y), 0],$$
$$\frac{\overline{h}_i}{H_0} = D_i + \frac{\mathrm{Ro}}{\mathrm{Bu}}\overline{\eta}_i(y), \quad (i = 1, 2), \quad (3.1)$$

where U is the velocity scale of the jet and H_0 is the total height at rest. The meridional coordinate y is rescaled by

TABLE 1. Realistic scales for midlatitude atmospheric jets.

f	L	U	H_1	H_2	g	θ_1	θ_2
10^{-4} s^{-1}	10^6 m	10 m s^{-1}	5 km	7 km	10 m s^{-2}	316 K	283 K

TABLE 2. Parameter values in the mc2RSW model.

f	L	U	H_0	g	D_1	$\alpha = \theta_2/\theta_1$
1	1	0.1	10	1	5/12	1.1

L, the width of the jet. The barotropic deformation radius in dimensional units is equal to $R_d = \sqrt{gH_0}/f$. We can also introduce nondimensional parameters: the Rossby number $\mathrm{Ro} = U/fL$, the barotropic Burger number $\mathrm{Bu} = R_d^2/L^2$, and the heights of the layers $D_i = H_i/H_0$.

Midlatitude atmospheric jets are usually close to the geostrophic balance. Typical parameters of atmospheric jets are given in Table 1, leading to the following characteristic numbers: $\mathrm{Ro} \approx 0.1$ and $\mathrm{Bu} \approx 10$. These can be mimicked in the mc2RSW model by the choice of the model parameters presented in Table 2. Note that nondimensional term U and H_0 coincide with Ro and Bu, respectively. We choose a balanced upper-layer Bickley jet configuration as our reference state. It is defined by

$$\overline{u}_1 = 0, \quad \overline{\eta}_1 = \frac{1}{\alpha - 1}\tanh(y) \quad \text{and} \tag{3.2}$$

$$\overline{u}_2 = \mathrm{sech}^2(y), \quad \overline{\eta}_2 = \frac{-1}{\alpha - 1}\tanh(y). \tag{3.3}$$

In this case, there is no deviation of the free surface, $\overline{\eta}_1 + \overline{\eta}_2 = 0$. Figure 2 shows the profiles of the dimensionless zonal velocity $\overline{u}_i$, thickness $\overline{\eta}_i$, and potential vorticity anomalies in each layer. The main gradients of PV have opposite sign (Fig. 2c), resulting in the strong baroclinic velocity $\overline{u}^{\mathrm{bc}} = \overline{u}_2 - \overline{u}_1 = \overline{u}_2$. Weak secondary PV gradients in the upper layer are observed at $y \approx \pm 0.4R_d$ (Fig. 2c), indicating that we have a mixed baroclinic/barotropic instability with a dominant baroclinic component.

b. Linear stability analysis

The system of Eqs. (2.1)–(2.3) can be linearized around the basic state [Eqs. (3.2)–(3.3)] in the case $P \equiv 0$. In that case, solutions can be sought in the form of normal modes $\propto \exp[i(kx - \omega t)]$ with the x wavenumber k and the angular frequency ω. We solve the associated eigenproblem for the eigenvalues $c = \omega/k$ by the pseudospectral collocation method[1] and obtain the phase diagram shown in Fig. 3. It represents the phase velocity $c_p = \mathcal{R}\{c\}$ and the growth rate $\sigma = \mathcal{I}\{c\}k$ of the unstable modes as a function of k (the stable modes are not shown).

The most unstable mode is marked by crosses and corresponds to a monopolar (in the across-jet direction) Rossby wave centered at the strong PV gradient of the jet (see Fig. 4). Its maximum dimensionless growth rate $\sigma = 0.27$ is reached at $k \approx 4.3R_d^{-1}$. For high wavenumbers ($k > 6R_d^{-1}$), its unstable branch splits in two, corresponding to a pair of stable monopolar Rossby modes. The unstable mode ($k \leq 6R_d^{-1}$) can then be understood as a resonance between these two modes, as usual in the layered models (Cairns 1979; Sakai 1989) or in classical quasigeostrophic baroclinic theory with counterpropagating waves propagation (Pedlosky 1979; Hoskins et al. 1985; Heifetz et al. 2004).

Figure 4 shows the geostrophic streamfunction in the lower layer $\psi_1 = g(\eta_1 + \eta_2)/f$ and in the upper layer $\psi_2 = g(\eta_1 + \alpha\eta_2)/f$ and the associated velocity field for the most unstable mode. The mode is obviously close to geostrophic balance and has a typical tilt between the upper- and the lower-layer vortices of the same sign, as predicted for quasigeostrophic baroclinic instability (Pedlosky 1979).

The second unstable mode (cf. Fig. 3) corresponds to a dipolar Rossby wave (not shown). It results from the resonance between two stable dipolar Rossby modes that appear at $k > 2R_d^{-1}$. One can think that they correspond to a barotropic instability, because their extrema are located along the change of sign of the PV gradient of the upper layer. Note that, for long-enough waves ($k < 0.75R_d^{-1}$), the corresponding growth rate is higher than the one of the monopolar Rossby mode.

These two modes are typical for jet instabilities (Hazel 1972), the slower mode (in terms of phase speeds)

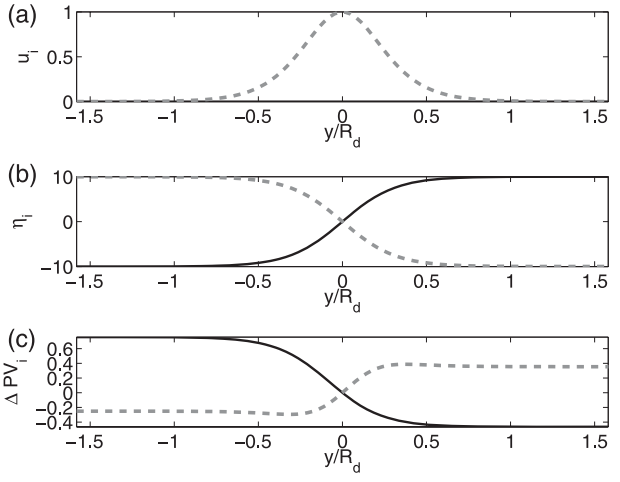

FIG. 2. Profile of the Bickley jet (Ro = 0.1 and Bu = 10): (a) zonal velocity $\overline{u}_i$, (b) thickness deviation $\overline{\eta}_i$, and (c) PV deviation $\Delta\mathrm{PV}_i$. Lower (upper) layer: solid black (dashed gray) line.

[1] Some details of the linear stability analysis may be found in appendix A.

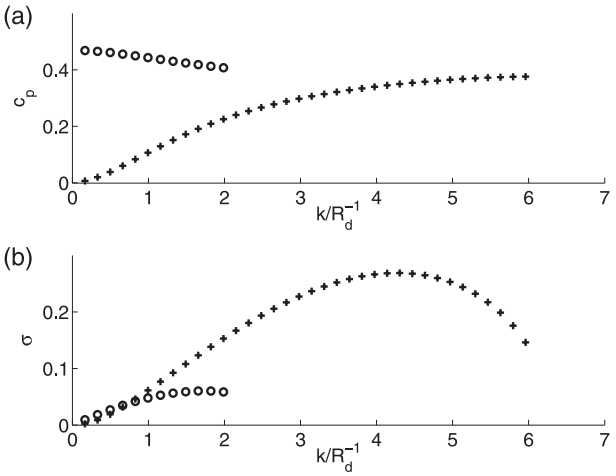

FIG. 3. Phase diagram resulting from the linear stability analysis of the baroclinic Bickley jet: (a) phase velocity c_p and (b) growth rate σ as a function of kR_d^{-1}. Crosses represent the most unstable mode, and open circles represent the second mode.

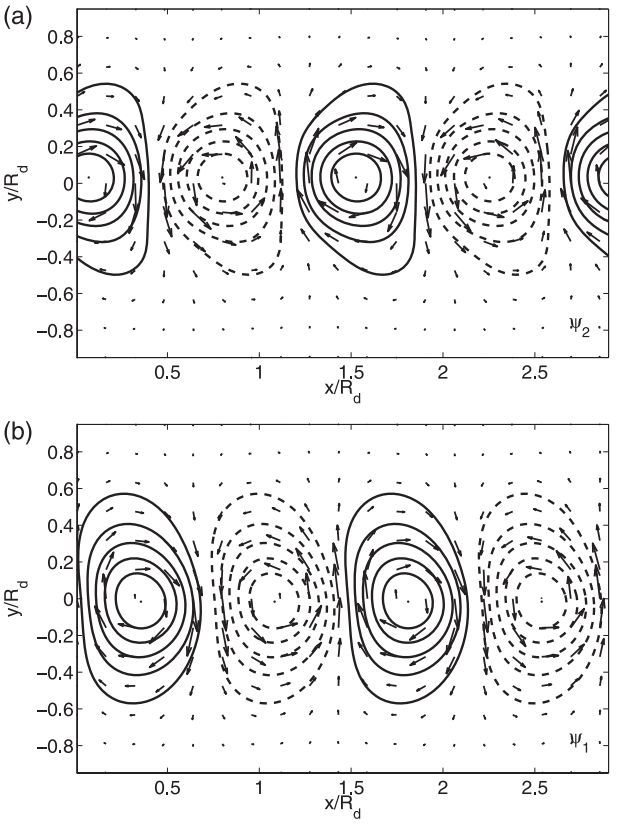

FIG. 4. Geostrophic streamfunctions in (a) the upper layer [$\psi_2 = g(\eta_1 + \alpha\eta_2)/f$] and (b) the lower layer [$\psi_1 = g(\eta_1 + \eta_2)/f$] for the most unstable mode $k = 4.3R_d^{-1}$. Positive (negative) values are represented by solid (dashed) lines, and the velocity field is represented by arrows. Scales are the same for both panels. Note that the domain is doubled in the x direction for better visualization.

producing a meandering perturbation of the jet (see Fig. 4) and the faster one giving a varicose perturbation (not shown). They can be distinguished by their kinetic energy, which is dominated by the baroclinic contribution for the former and the barotropic contribution for the latter (not shown). This confirms that the first mode should be related to the baroclinic instability, whereas the second mode should be related to the barotropic instability.

4. Numerical setup

The linear stability analysis of the previous section allows us to identify the most unstable perturbation for the mc2RSW model in subsaturated conditions ($P \equiv 0$). This perturbation is now used to initialize the nonlinear numerical simulations in order to study the effects of moisture and condensation on the nonlinear development of the instability.

We use a robust well-balanced finite-volume scheme for the multilayer shallow-water system proposed by Bouchut and Zeitlin (2010), where we add the equation of the conserved tracer Q and condensation as a conditional source/sink [see appendix C of Bouchut et al. (2009)]. In the simulations below the spatial domain is $L_x \times L_y = 4.6 \times 20$ in the units of length L (jet width). The barotropic deformation radius $R_d = \sqrt{\mathrm{Bu}}L \approx 3.16L$ is the intrinsic length scale of the model with rotation and is then used as the unit of length in the figures. This means that $L_x \approx 1.45R_d$ and $L_y \approx 6.32R_d$. The zonal domain length L_x is chosen to be equal to the wavelength of the most unstable mode ($k \approx 4.3R_d^{-1}$). Thus, possible subharmonic instabilities are filtered. Note that in the figures that follow the zonal domain is doubled for better visualization. The time scale is chosen to be the inverse of the inertial frequency, $T_i = f^{-1}$.

We choose the same resolution ($0.1L \approx 0.03R_d$) in the zonal and meridional directions, $n_x = 46$ and $n_y = 200$ points. The time step is chosen as the minimum between a specific value allowing to respect the Courant–Friedrich–Levy (CFL) condition Δt^{CFL} and some maximum value $\Delta t^{\max}$ (chosen to be $\pi/5f$) imposed to avoid a too-coarse resolution in time. We use periodic conditions at the zonal ($x = \pm L_x/2$) and Neumann conditions at the meridional ($y = \pm L_y/2$) boundaries. Even if these conditions do not completely exclude complex reflections of the solutions and numerical dissipation at the boundaries, such effects are weak far from the boundaries and do not significantly affect our simulations.

The relaxation time in the precipitation parameterization [Eq. (2.5)] is linked to the time step of the numerical scheme $\tau = 5\Delta t$ and corresponds to a rapid (quasi immediate) relaxation. This choice allows to avoid numerical instabilities, which may occur when

$\tau \to \Delta t$. The other parameters related to moisture are $\beta = 1$ and $Q^s = 0.3H_0$. They control the linear internal gravity wave speed c_g in precipitating regions in the immediate relaxation approximation $\tau \to 0$ (see Lambaerts et al. 2011b). The ratio of the moist static stability and the dry one N_m/N_d in our model can be approximately given by the ratio of the internal wave speeds $c_g^{P>0}/c_g^{P=0}$. With our choice of moist parameters, the value of this ratio (~0.5) is close to observations: using Eq. (11) of O'Gorman (2011), we obtain $N_m/N_d = \sqrt{1-(1-N_{\text{eff}}^2/N_d^2)/\lambda}$, where $\lambda \approx 0.6$ and the effective static stability $N_{\text{eff}}^2/N_d^2 \approx 0.55$ for midlatitudes. For simplicity, we choose a uniform initial moisture field. Its value $Q_0 = 0.299H_0$ is close enough to Q^s, so that condensation will be triggered during the exponential growth of the perturbation. Such background moisture is referred to as quasi saturated, because the relative deficit of moisture is weak, $1 - Q_0/Q^s \approx 3.3\%$. Two types of simulations are presented below: a dry one for which condensation is switched off and a moist one for which condensation may be triggered beyond the saturation threshold.

5. Initial stages of the instability

The development of the instability is examined by imposing a small-amplitude unstable perturbation onto the background jet (of order 10^{-4} in dimensionless units) at initial time. In that case, the dry DNS should exhibit the exponential growth with a rate predicted by the linear stability analysis at the initial stages. If observed, this will benchmark our nonlinear numerical simulation. We also expect that advection of moisture will lead, at some moment, to oversaturation and hence to condensation in some locations, which will supposedly modify the predictions of the linear stability analysis. Thus, our main concerns at the initial stage are the growth of perturbations in the dry and precipitating cases and the influence of the growing mode upon the distribution of the moisture field in view of triggering the precipitation. It should be noted that, in spite of the balanced character of the initial configuration, a readjustment of the flow occurs at the very early stages ($t < 40T_i$), due to the discretization errors. It results in the weak emission of inertia–gravity waves (IGW) from the jet, as explained in appendix B.

a. Exponential growth of the perturbation

To quantify the instability, we need to define an appropriate norm of the perturbation. We choose to work with the dry energy norm,

$$s^2(t) = \int\int \left[\sum_{i=1}^{2} H_i \frac{\boldsymbol{v}_i'^2}{2} + g\frac{(\eta_1' + \eta_2')^2}{2} + g(\alpha - 1)\frac{\eta_2'^2}{2} \right] dx\, dy. \tag{5.1}$$

The prime denotes the anomaly of the corresponding quantity with respect to its value in the basic state defined by Eqs. (3.2) and (3.3). The first term in the rhs corresponds to kinetic energy, whereas the sum of the last two terms represents potential energy related to the perturbations of the free surface $\eta_1' + \eta_2'$ and of the interface between the layers η_2'.

This norm is dry in the sense that it does not take into account the moisture anomaly $Q - Q_0$. A moist energy norm (which would be conserved for small perturbations about the state of rest) defined for the one-layer mcRSW model (Lambaerts et al. 2011a) does not allow direct extrapolation to the two-layer model.[2] It should be stressed that, in order to quantify the growth of the perturbations with respect to the steady flow from which they extract their energy, we choose to measure the norm of the perturbation with respect to the basic state. The norm of the deviation from the mean zonal state can also be considered but is not very instructive as the latter is affected by condensation.

The evolution of the dry energy norm (5.1) is obtained from the mc2RSW equations (2.1)–(2.3), where all nonprecipitating terms and the factor $(\boldsymbol{v}_1 - \boldsymbol{v}_2)/h_2$ of the last term of Eq. (2.2) are linearized about the background jet $(\overline{u}_i, H_i + \overline{\eta}_i)$. After some algebra, we get

$$\frac{ds^2}{dt} = -\int\int H_2 u_2' v_2' \partial_y \overline{u}_2\, dx\, dy + \int\int \frac{f^2}{g}\frac{\overline{u}_2 - \overline{u}_1}{\alpha - 1}\psi'^{\text{bc}}\partial_x \psi'^{\text{bt}}\, dx\, dy + \int\int f\overline{\eta}_1(\boldsymbol{v}_1' \cdot \nabla\psi_1' - \boldsymbol{v}_2' \cdot \nabla\psi_2')\, dx\, dy$$
$$+ \int\int (\overline{u}_2 - \overline{u}_1)u_2'\beta P\, dx\, dy + \int\int f\psi'^{\text{bc}}\beta P\, dx\, dy. \tag{5.2}$$

Here, ψ'^{bt} and ψ'^{bc} are the barotropic and baroclinic streamfunctions defined by $\psi'^{\text{bt}} = D_1\psi_1' + (1 - D_1)\psi_2'$ and $\psi'^{\text{bc}} = \psi_2' - \psi_1'$, respectively. The baroclinic streamfunction roughly corresponds to the potential temperature in standard QG models (Pedlosky 1979; Holton 1972). In particular, we have $\psi'^{\text{bc}} = g(\alpha - 1)\eta_2'/f$, which shows how the baroclinic streamfunction is related to the interface

[2] One can mention however attempts to deal with such a norm in the two-layer quasigeostrophic model (Lapeyre and Held 2004).

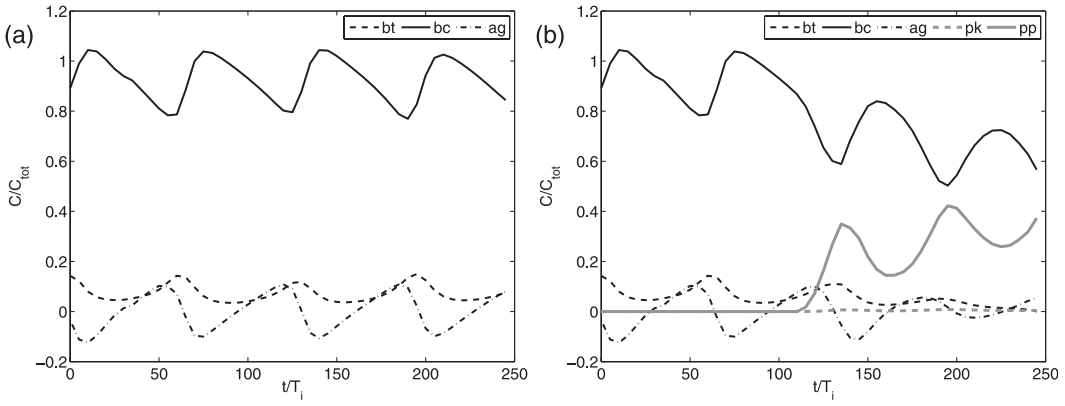

FIG. 5. Contributions to the energy budget [Eq. (5.2)] for the perturbations: (a) dry and (b) moist simulations. The dashed black line is the barotropic extraction term, the solid black line is the baroclinic extraction term, the dashed–dotted black line is the ageostrophic term, the dashed gray line is the momentum transfer by mass exchange, and the solid gray line is the production of APE by condensation.

height. We remind that $\psi_1' = g(\eta_1' + \eta_2')/f$ and $\psi_2' = g(\eta_1' + \alpha\eta_2')/f$ are the geostrophic streamfunctions.

This kind of budget allows us to make a link with the standard decomposition of the energy production for the baroclinic/barotropic conversion (Pedlosky 1979). The first term on the rhs of Eq. (5.2) is the extraction of eddy kinetic energy from the mean zonal flow $\overline{u}_2$ through barotropic instability. The second term is the extraction of eddy potential energy from the basic state through the baroclinic instability. The third term is an ageostrophic source in the sense that it disappears at the zeroth order in Rossby number, $\boldsymbol{v}_i = \mathbf{k} \times \nabla\psi_i + O(\mathrm{Ro})$.

The last two terms on the rhs of Eq. (5.2) are conditioned by the latent heat release. The first one corresponds to a kinetic energy source (or dissipation) because of the momentum transfer induced by the mass flux βP from the lower layer to the upper one. Its contribution depends on the background vertical shear $\overline{u}_1 - \overline{u}_2$ and the perturbation of the upper-layer velocity field u_2'. The second term corresponds to a potential energy source due to precipitation. This term is positive when the correlation between condensation and ψ'^{bc} (related to the potential temperature of the layer) is positive (see Lorenz 1955; Lapeyre and Held 2004).

Figure 5 presents the detailed energy budget normalized by the sum of all contributions for the dry and moist simulations. In the dry and moist simulations, it is the baroclinic extraction of potential energy from the mean flow that dominates, which is classical for the baroclinic instability. There is a small barotropic extraction from the mean flow as well, showing that the instability is of a mixed type. The ageostrophic term works either as a source or a sink of energy. Its oscillations are in phase opposition with the ones of the baroclinic energy conversion term. Concerning the moist simulation (Fig. 5b), after $t = 120T_i$, the generation of APE by latent heat release starts to rise to large values, with oscillations in phase opposition with the oscillations of the baroclinic term. The oscillations observed in this term are an artifact of the normalization by the sum of all the contributions as the nonnormalized generation by latent heat release increases almost exponentially in time (not shown). At the same time, the contribution of the nonprecipitating terms to the total budget decreases. The momentum transfer term due to the mass exchange is mostly positive (not shown) but almost negligible in the budget.

Figure 6 compares the exponential growth rate of the energy norm [Eq. (5.1)],

$$\sigma(t) = \frac{1}{2}\frac{d}{dt}\ln\left[\frac{s^2(t)}{s^2(t_0)}\right], \tag{5.3}$$

in the dry and the moist simulations for t up to $500T_i$. At the initial stages, after the readjustment process ($t > 40T_i$), the growth rate in the dry simulation stabilizes around $\sigma^d \approx 0.25\mathrm{Ro}T_i^{-1}$ close to the value obtained from the linear stability analysis ($\approx 0.27\mathrm{Ro}T_i^{-1}$). The small difference probably results from the nonlinearity of the numerical simulation, which allows a transfer of energy to the higher modes with smaller wavelengths (the discretization errors may also play a role). In the moist simulation, we observe the same growth rate as in the dry case until $t \approx 100T_i$. Then, a sudden increase in the growth rate, which reaches a value of $\sigma^m \approx 0.33T_i^{-1}$ at $t \approx 180T_i$ (+32% with respect to the dry one), takes place. It corresponds to the time when precipitation is in action. This is in agreement with previous studies (e.g., Emanuel et al. 1987) and may be explained by the action of the potential energy source represented by the last

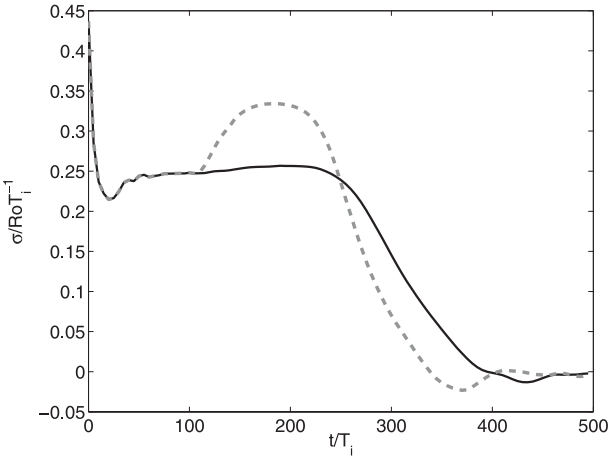

FIG. 6. Exponential growth rate σ of the perturbation in the dry (solid black line) and moist (dashed gray line) simulations.

term on the rhs of Eq. (5.2). Note that the coefficient β strongly influences the value of the growth rate, as discussed at the end of appendix C.

After $t \approx 220T_i$ in the dry simulation and $t \approx 200T_i$ in the moist simulation, the growth rate decreases as the nonlinear saturation of the instability starts. Thus, in the moist case, precipitation accelerates the instability cycle.

b. Growth of the moisture anomalies

The study of the growth rate of the instability in the dry and moist simulations has highlighted the role of production of APE by diabatic heating. This process can be modulated by the spatial correlation between the precipitation and the baroclinic streamfunction. To understand this, we need to consider the spatial distribution of the moisture anomalies. At the very early stages ($t \approx 5T_i$), weak moisture anomalies are created by the lower-layer divergence (Fig. 7a). We can clearly see the trace of the IGW emitted during the geostrophic readjustment. These weak anomalies do not significantly affect the subsequent evolution. Stronger moisture anomalies develop in the jet at the vortex periphery and grow together with the unstable mode (Figs. 7a,b). Rapidly, their spatial patterns are out of phase with the divergence patterns (not shown). They approximately correspond to that of the relative vorticity $\zeta_1 = \partial_x v_1 - \partial_y u_1$ (Fig. 7b): positive/negative moisture anomalies are mainly confined in cyclones ($\zeta_1 > 0$)/anticyclones ($\zeta_1 < 0$).[3] This can be easily explained by linearizing Eq. (2.4) and the vorticity equation following from Eq. (2.2),

$$\partial_t Q' + Q_0 \nabla \cdot \boldsymbol{v}_1' = 0 \quad \text{and} \tag{5.4}$$

$$\partial_t \zeta_1' + f \nabla \cdot \boldsymbol{v}_1' = 0. \tag{5.5}$$

Moisture anomalies $Q - Q_0$ are thus formed by the convergence in the lower layer $\nabla \cdot \boldsymbol{v}_1$ whence

$$Q'(x,y,t) = \frac{Q_0}{f}[\zeta_1'(x,y,t) - \zeta_1'(x,y,0)], \tag{5.6}$$

there are no moisture anomalies initially. This result indicates that moisture and vorticity will be strongly correlated at the initial stage of the instability, once $\zeta_1'(x,y,t)$ becomes dominant in the rhs of Eq. (5.6). Precipitation is thus expected to be triggered in the cyclonic areas. During the linear stage, the correlation rapidly reaches a value close to 1 (Fig. 8) in both moist and dry simulations. This remains true during the whole initial stage. However as can be seen in Fig. 7c, in the moist case there is an asymmetry between low positive values and high negative values of moisture anomalies that develops. This is due to condensation as it removes water vapor in the regions where it reaches saturation. In the dry simulation, this is not the case (not shown).

6. Nonlinear saturation of the instability

For later times ($t > 250T_i$), the structure of the perturbation changes under the influence of the hydrodynamic nonlinearity. The baroclinic wave breaks and a significant reorganization of the flow takes place. This reorganization essentially depends on the balanced dynamics associated with the wave breaking. It leads to the generation of relatively important ageostrophic motions, as we will see below.

a. Saturation in terms of the perturbation norms

To understand the difference in the nonlinear saturation of the simulations with and without precipitation, we first compare the evolution of different norms of the perturbation. As in section 5, we measure the perturbation with respect to the initial jet because the baroclinic Bickley jet is a steady solution of the system.

Figure 9 shows the dry energy norm [Eq. (5.1)] and its potential component [two last terms of Eq. (5.1)] in the dry and moist simulations. In both simulations, these norms start to grow exponentially, as predicted for the linear stage of the instability. After reaching their respective maxima, the norms decrease to a saturated value. In the moist case, the development of the instability is accelerated and the norms reach their maxima earlier ($t = 340T_i < 400T_i$) and at a higher value ($s_m^2/s_d^2 - 1 \sim 13\%$). If the dry energy norm saturates at long times at a higher

[3] The lower-layer relative vorticity ζ_1 can be coarsely deduced from the lower-layer velocity field $\boldsymbol{v}_1$ (arrows) in Fig. 7 (right), because the unstable perturbation is close to the geostrophic balance.

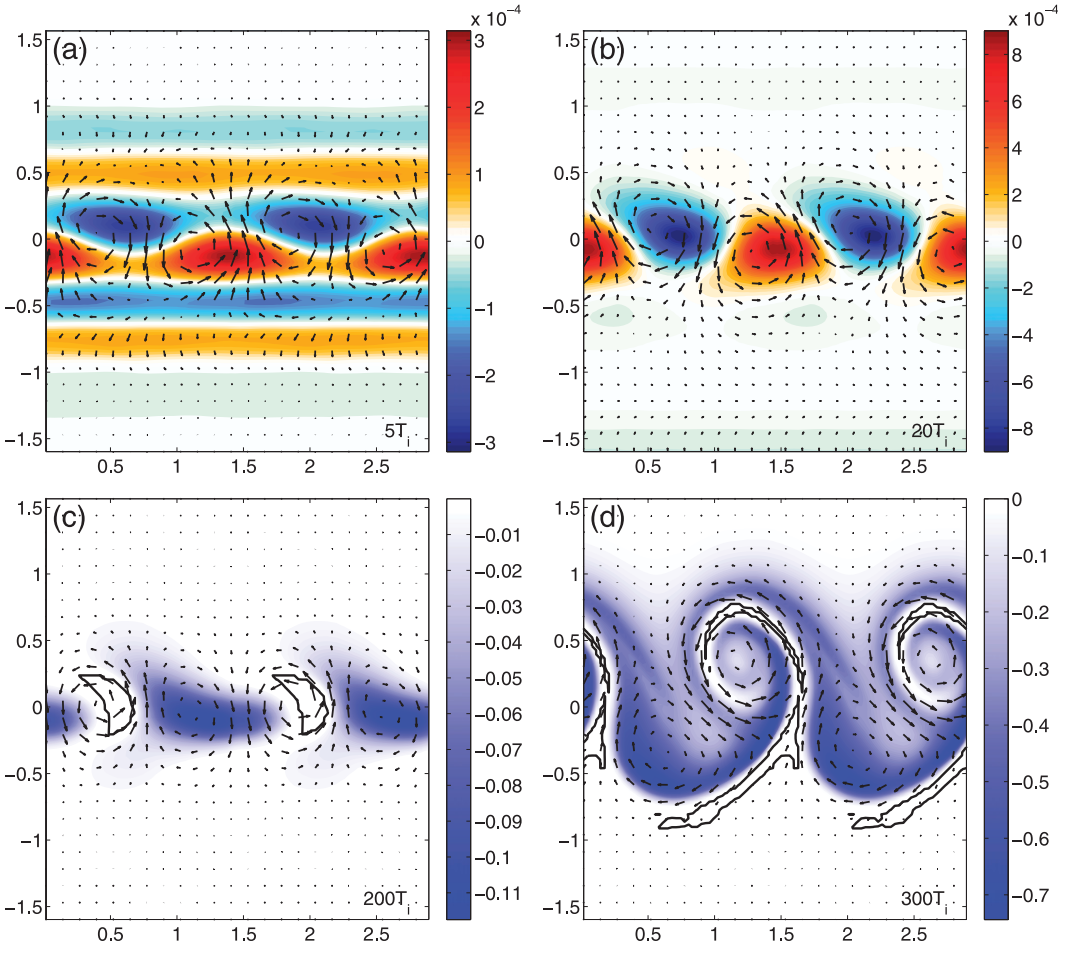

FIG. 7. Moisture anomaly $Q - Q_0$ at different times for the moist simulation. Lower-layer velocity $\boldsymbol{v}_1$ is superimposed. Time (a) $t = 5T_i$, (b) $t = 20T_i$, (c) $t = 200T_i$, and (d) $t = 300T_i$. Precipitating regions are delimited by thick black contours. Note that the color scale changes from panel to panel.

value in the moist case, its value stays close to that of the dry case, $s_m^2/s_d^2 - 1 \sim 4.5\%$. This is in contrast with the results for the barotropic instability in the one-layer mcRSW model (Lambaerts et al. 2011a). One can assume that this difference essentially comes from the total mass conservation of the mc2RSW model, which is not satisfied in the one-layer case. Such behavior is also visible in the potential energy norm with a weaker difference between the dry and the moist saturated values (<1%). It should be stressed that the total and potential (dry) energies of the system strongly increase due to condensation, so that their values at the new equilibrium state clearly differ between the dry and the moist simulations.

The evolution of the kinetic energy norm s_k^2 and of the total enstrophy norm

$$s_\zeta^2 = \frac{1}{2}\int\int (\zeta_1^2 + \zeta_2^2)\, dx\, dy \tag{6.1}$$

is given in Fig. 10 and follows that of the previous ones. A second maximum appears at $t = 450T_i$, as in the norm of ageostrophic motions (see below). It corresponds to the reorganization of the flow discussed in the next section. This reorganization is accompanied by the emergence of a precipitating region. The difference between dry and moist saturated values of the kinetic energy norm is of the same order (~9%) as for the dry energy norm, whereas for the enstrophy norm this difference is stronger (~30%) because of the significant intensification of the cyclones in the lower layer (see below).

In conclusion, condensation temporarily enhances the efficiency of the baroclinic instability and accelerates its development. Only weak differences in the norms of the perturbation appear at saturation. Note that these differences can be stronger if evaporation is included (not shown). In fact, evaporation would tend to maintain precipitation such that the equilibration of the flow is

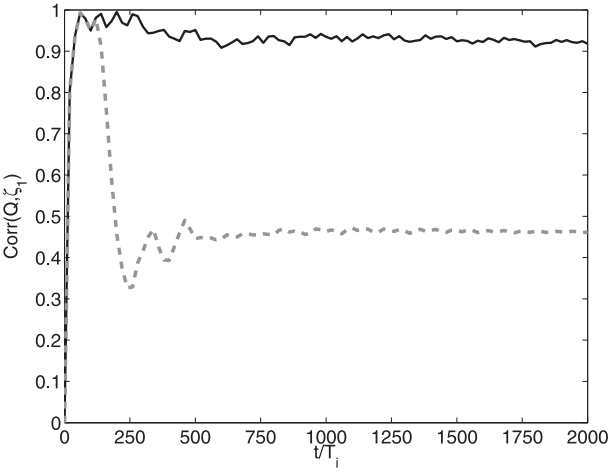

FIG. 8. Evolution of the correlation between lower-layer vorticity $\zeta_1 = \partial_x v_1 - \partial_y u_1$ and moisture anomaly $Q - Q_0$ as a function of time for the dry (solid black line) and moist (dashed gray line) simulations.

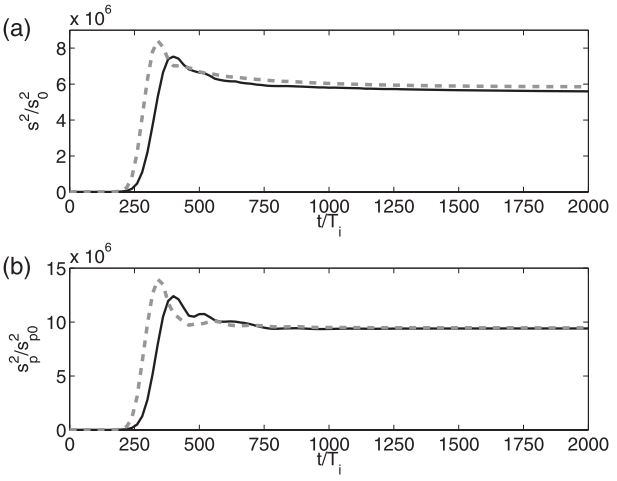

FIG. 9. (a) Dry energy s^2 and (b) potential energy s_p^2 norms of the perturbation in the dry (solid black line) and moist (dashed gray line) simulations.

permanently altered allowing the perturbation to continue to grow.

b. Balanced motions during the saturation

1) WAVE BREAKING

Figure 11 shows the evolution of the relative vorticity fields ζ_1 and ζ_2 at different times $t = \{200T_i; 250T_i; 300T_i; 350T_i\}$ in the dry and the moist simulations. In the dry simulation, the initially aligned lower-layer cyclones ($\zeta_1 > 0$) and anticyclones ($\zeta_1 < 0$) start to shift at $t \approx 250T_i$ northward and southward, respectively (Fig. 11c). At the same time, the isolines of the upper-layer relative vorticity ζ_2 reconnect to form cyclonic and anticyclonic vortices. The intensity of these structures increases in an asymmetric way, with cyclones more intense than the anticyclones. For $t \geq 300T_i$, the wave breaks forming strong gradients at the eastern side of the upper-layer cyclones (Figs. 11e,g). The moisture anomaly displays strong drying along the cold front. This kind of wave breaking is consistent with the so-called cyclonic wave breaking (CWB) and the life cycle of the second type (LC2) of unstable baroclinic waves (e.g., Thorncroft et al. 1993). Moreover, this nonlinear development is close to one obtained with numerical semigeostrophic models, such as the full jet case of Hoskins and West (1979) or the cyclonic-shear jet case of Davies et al. (1991).

In the moist simulation, the nonlinear development of the instability is accelerated since the wave has grown faster because of the latent heat release (cf. section 5). The dimensionless "growth time" $t^\star = \sigma t$ (where σ is the growth rate) can be used to compare the growth of the perturbation in the dry and moist simulations. Thus, the time $t^\star \approx 44$ corresponds to $t = 300T_i$ (Fig. 11e) for the dry simulation and to $t = 250T_i$ (Fig. 11d) for the moist simulation. The time $t^\star \approx 18$ corresponds to $t = 350T_i$ (Fig. 11g) for the dry simulation and to $t = 300T_i$ (Fig. 11f) for the moist simulation. The precipitating regions emerge in the frontal part of the lower-layer cyclones. They progressively form a "tongue" or a "comma" shape at $t = 250T_i$ (Figs. 11d, 7d). This is in a stunning correspondence, for such a simple model, with sub-synoptic-scale comma clouds, well known from the observations of midlatitude synoptic perturbations (e.g., Browning 1986; Bluestein 1993).

Condensation significantly increases the relative vorticity in the lower layer as follows from the potential vorticity equations (2.7) and (2.8). Moreover, a strong correlation exists between the evolution of the relative vorticity in the lower layer,

$$(\partial_t + \boldsymbol{v}_1 \cdot \nabla)\zeta_1 = -(\zeta_1 + f)\nabla \cdot \boldsymbol{v}_1, \qquad (6.2)$$

and the precipitation in the immediate relaxation approximation,

$$P_{\tau \to 0} = -Q^s \nabla \cdot \boldsymbol{v}_1 > 0, \qquad (6.3)$$

via the convergence field $\nabla \cdot \boldsymbol{v}_1 < 0$. Consequently, the cyclones in the lower layer are locally intensified ($t = \{200T_i, 250T_i\}$). This local intensification is in agreement with the previous numerical results of Balasubramanian and Yau (1994), who worked with a two-layer primitive equation model with parameterized slantwise convection. Later (for $t \geq 300T_i$), the intensity of precipitation becomes weaker and the cyclone/anticyclone asymmetry

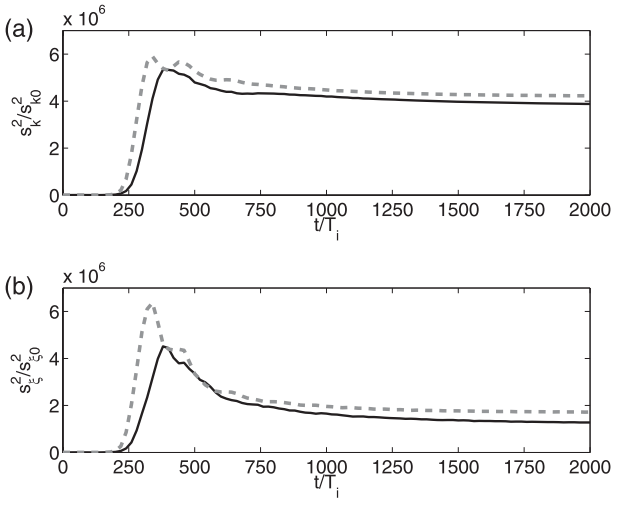

FIG. 10. (a) Kinetic energy s_k^2 and (b) enstrophy s_ξ^2 norms of the perturbation in the dry (solid black line) and moist (dashed gray line) simulations.

persists without significantly modifying the main spatial structure observed in the dry case (cf. Figs. 11f,g).

2) VORTEX ASYMMETRY

The cyclone–anticyclone asymmetry observed during the cyclonic wave breaking can be quantified using the skewness of the relative vorticity ζ_i, $\mathcal{S}_i = \langle \zeta_i^3 \rangle / (\langle \zeta_i^2 \rangle)^{3/2}$, where $\langle \cdot \rangle$ denotes spatial average and $i = 1, 2$ is the index of the layer. The evolution of the skewness is presented in Fig. 12 for both layers in the dry and moist simulations.

At the initial stage ($t < 200T_i$), there is no clear asymmetry between cyclones and anticyclones in the dry simulation. This means that the baroclinic instability develops in the quasigeostrophic regime. At $200T_i < t < 400T_i$, the cyclonic vorticity is favored ($\mathcal{S}_i \sim 0.5$) in both layers for the dry case. This is consistent with the cyclonic wave breaking that we already observed on Fig. 11. Afterward (during the vortex street formation; see below), the upper layer shows an anticyclonic preference, whereas in the lower layer the asymmetry is small.

In the moist case, the asymmetry between cyclone and anticyclone is manifest in the lower layer when condensation is triggered ($100T_i < t < 350T_i$; see Fig. 18b) with a skewness toward cyclonic vorticity ($\mathcal{S}_1 \sim 6$). In the upper layer, we also observe a positive skewness, as in the dry case. Note that, if we were to not take into account the zonal flow when calculating the relative vorticity, we would obtain a skewness close to 3.5 in the lower layer and -1.5 in upper layer at time around $t \approx 250T_i$. After $t > 250T_i$, the skewness decreases rapidly toward anticyclonic values. This transition occurs faster than in the dry case.

To explain this behavior, we can rely on the potential vorticity equations (2.7) and (2.8), which show that latent heat release increases PV in the lower layer and decreases it in the upper layer. Initially, there is no relative vorticity in the lower layer. It can be expected that the change in PV due to latent heat release will traduce in a change in vorticity, so that cyclonic vorticity will be created in the lower layer. Moreover, condensation is coupled with divergence and velocity for the lower layer [through the moisture equation (2.4)], which exerts a positive feedback. This explains why we obtain positive skewness in this layer. On the contrary, in the upper layer, the initial Bickley jet has a nonzero vorticity distribution. As can be seen in Fig. 11, the condensation does not develop along these nonzero relative vorticity anomalies. The relative vorticity anomalies that form in the upper layer are vertically tilted with the ones in lower layer in order to the baroclinic instability to occur. This explains why the vorticity skewness remains positive in the upper layer (whereas the skewness of the nonzonal vorticity is negative).

The result on the nonzonal relative vorticity is similar to what Lapeyre and Held (2004) obtained in the case of moist baroclinic turbulence. Here, it is obtained only for a single baroclinic life cycle, whereas their study considered a statistical equilibrium turbulent field.

Finally, the effective static stability which depends on asymmetry between upward and downward motions can be another tool to characterize the role of condensation in the asymmetry between cyclones and anticyclones. We found that the asymmetry parameter λ introduced by O'Gorman (2011) is close to 0.5 all over the dry simulations, confirming that there is no clear asymmetry in the dry setting. In the moist simulation, λ reaches 0.85 during the time when precipitation occurs and then decreases toward 0.5. We therefore see that moisture does have an effect on the effective static stability and on the baroclinic perturbations, whereas the area of precipitating region is quite reduced in this case.

3) VORTEX STREET FORMATION

For later times ($t \geq 350T_i$), the flow is reorganized, tending to form a vortex street along the initial jet axis (Fig. 13). In both simulations, when cyclones and anticyclones roll up, a part of the anticyclone (cyclone) is swept away to the north (south) by a cyclone (anticyclone) (see Fig. 13a). These appear as vorticity anomalies with respect to the main vortex street.

In the dry simulation, the vorticity anomalies are ejected in the form of asymmetric vortex dipoles. Figure 13a shows the northwestward ejection of a dipole resulting from the northern anomaly of anticyclonic motions at $t = 400T_i$. This dipole is mostly anticyclonic, especially in the upper layer such that it reverses the vortex asymmetry in this latter (see Fig. 12a). The dipoles

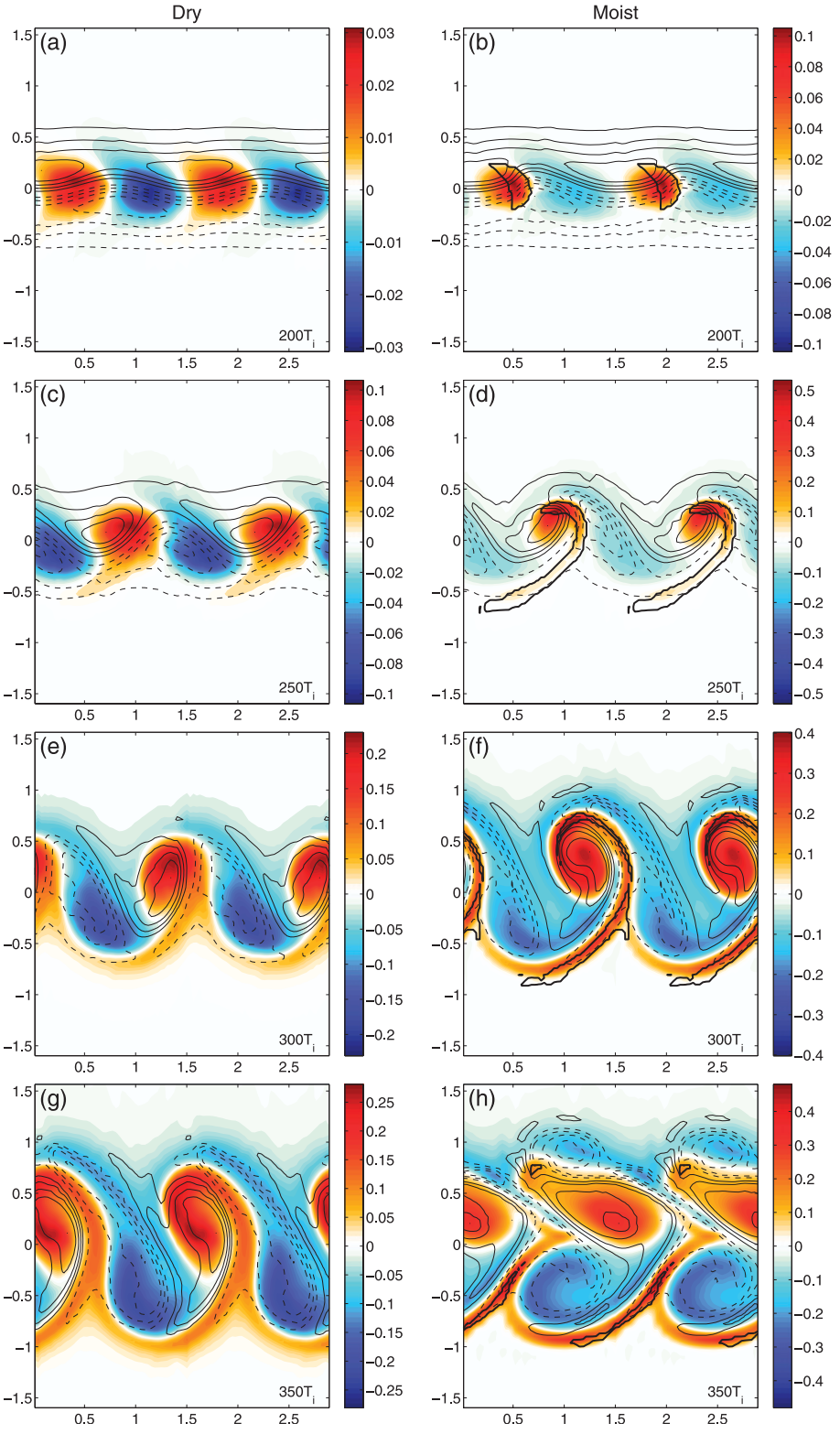

FIG. 11. Lower-layer (colors) and upper-layer relative vorticity $\zeta_i = \partial_x v_i - \partial_y u_i$ during the nonlinear development of the instability for the (a),(c),(e),(g) dry and (b),(d),(f),(h) moist simulations: (a),(b) $t = 200T_i$; (c),(d) $t = 250T_i$; (e),(f) $t = 300T_i$; and (g),(h) $t = 350T_i$. Thin solid (dashed) contours represent positive (negative) values. Precipitating regions are delimited by thick black contours. Note that the color scale changes from panel to panel.

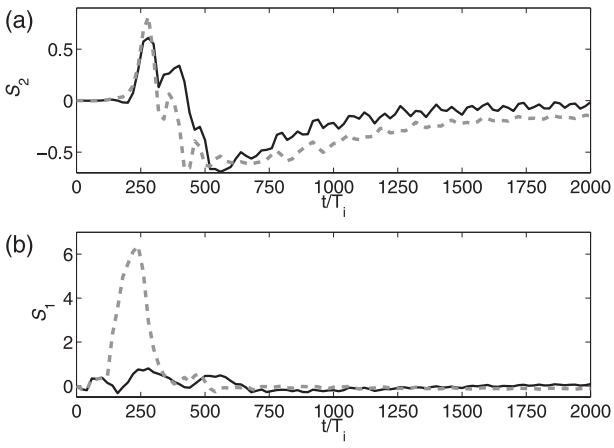

FIG. 12. Skewness of the relative vorticities in (a) the upper and (b) the lower layers in the dry (solid black line) and moist (dashed gray line) simulations.

then stabilize forming a secondary vortex street. Later (at $t = 800T_i$), a southwestward dipole ejection also occurs resulting in a reorganization of the main anticyclone in contact with the remaining southern cyclonic anomaly (see Fig. 13c). As to the first dipole, the ejection leads to a secondary vortex street formation. Consequently, the new equilibrium state reached by the flow is composed of three vortex streets: the main one in the center of the domain and the northern and the southern secondary ones.

In the moist simulation, the ejection of the first dipole is accelerated (Fig. 13b) starting at $t \approx 350T_i$ (see Fig. 11h). This accelerated ejection can be observed in Figs. 11c–f of Balasubramanian and Yau (1996), who simulated primitive equations with moisture as a tracer. During ejection (at $t \approx 450T_i$), a region of moderate precipitation emerges at the front of the cyclone (not shown). As shown in Fig. 13d, no secondary ejection is observed at $t = 800T_i$. In fact, the cyclonic perturbation in the upper layer around $x = 0.5R_d$ and $y = -0.85R_d$ in Fig. 13b is not sufficiently strong to persist as a coherent vortex. As a consequence, it cannot form a dipole with the anticyclone and escape. At later stages, the flow is being progressively stabilized in the form of vorticity bands.

4) MODIFICATION OF THE MEAN ZONAL JET

The formation of the main vortex street directly modifies the mean zonal jet and the equilibration of the vorticity anomalies. Figure 14 shows the position of the three first extrema of the mean zonal velocity in the upper and the lower layers $\langle u_i \rangle_x(y, t)$, where $\langle \cdot \rangle_x$ denotes the zonal average.

In the dry simulation, the initial westerly upper-layer jet starts to shift southward until $t \approx 450T_i$ (Fig. 14a) and extends to the lower layer, becoming barotropic (Fig. 14b). Again, this is consistent with the classical baroclinic LC2 (Thorncroft et al. 1993), which is properly reproduced in our simple model: the CWB produces negative momentum fluxes $\langle u_i v_i \rangle_x$ in the jet core, which induces a southward shift of the initial upper-layer jet and the emergence of an associated lower-layer jet. After $t \approx 450T_i$, the resulting barotropic jet becomes unstable and is shifted northward such that it stabilizes at $y = -0.18R_d$. The ejection of the first dipole leads to formation of a barotropic northern easterly jet, which stabilizes at $y = 0.95R_d$ (Figs. 14a,b). A southern easterly jet also forms at $y = -0.95R_d$ for $400T_i < t < 600T_i$ because of the presence of the southern cyclonic anomaly. It is mostly baroclinic, is more intense in the lower layer, and presents potential vorticity gradients of opposite sign (not shown). It eventually becomes unstable at $t \approx 600T_i$ and is shifted southward as the dipole is ejected. It finally stabilizes at $y = -1.4R_d$.

In the moist simulation, the southward shift of the initial westerly jet and its barotropization occur earlier, at $t \approx 230T_i$ (Figs. 14a,b). It is rapidly followed by a northward shift such that the main jet stabilizes at a higher latitude (around $y \approx 0R_d$) than in the dry case. The two easterly jets also stabilize at higher latitudes, especially the southern one because no intense dipole ejection occurs. The distance between the westerly and the southern easterly jets is reduced compared to the dry case. In parallel, PV homogenization (in the lower layer) is more spatially confined in the moist simulation (not shown).

Figure 15 shows zonally averaged zonal velocity in the lower and upper layers at very long times ($t = 2000T_i$) for the dry and the moist simulations. These profiles are superimposed onto the initial one for comparison. At this time, vortices are almost indistinguishable. The amplitude of the main jet increases in the moist case with respect to the dry one. This tendency is similar for the northern easterly jet, whereas it is less clear for the southern one. The amplification of the lower-layer jets is in agreement with the results of Balasubramanian and Garner (1997) obtained with a numerical primitive equations model on the sphere including simplified slantwise convection as in Emanuel et al. (1987). The associated lower-layer PV gradients increase in the moist case as a consequence of the vortex asymmetry induced by condensation (not shown).

c. *Generation of ageostrophic motions*

Latent heat release has been shown to essentially modify the saturation phase of the baroclinic instability. It arises in frontal cyclonic regions in the lower layer and affects the divergent motions. These motions are ageostrophic in essence and can be easily diagnosed in the

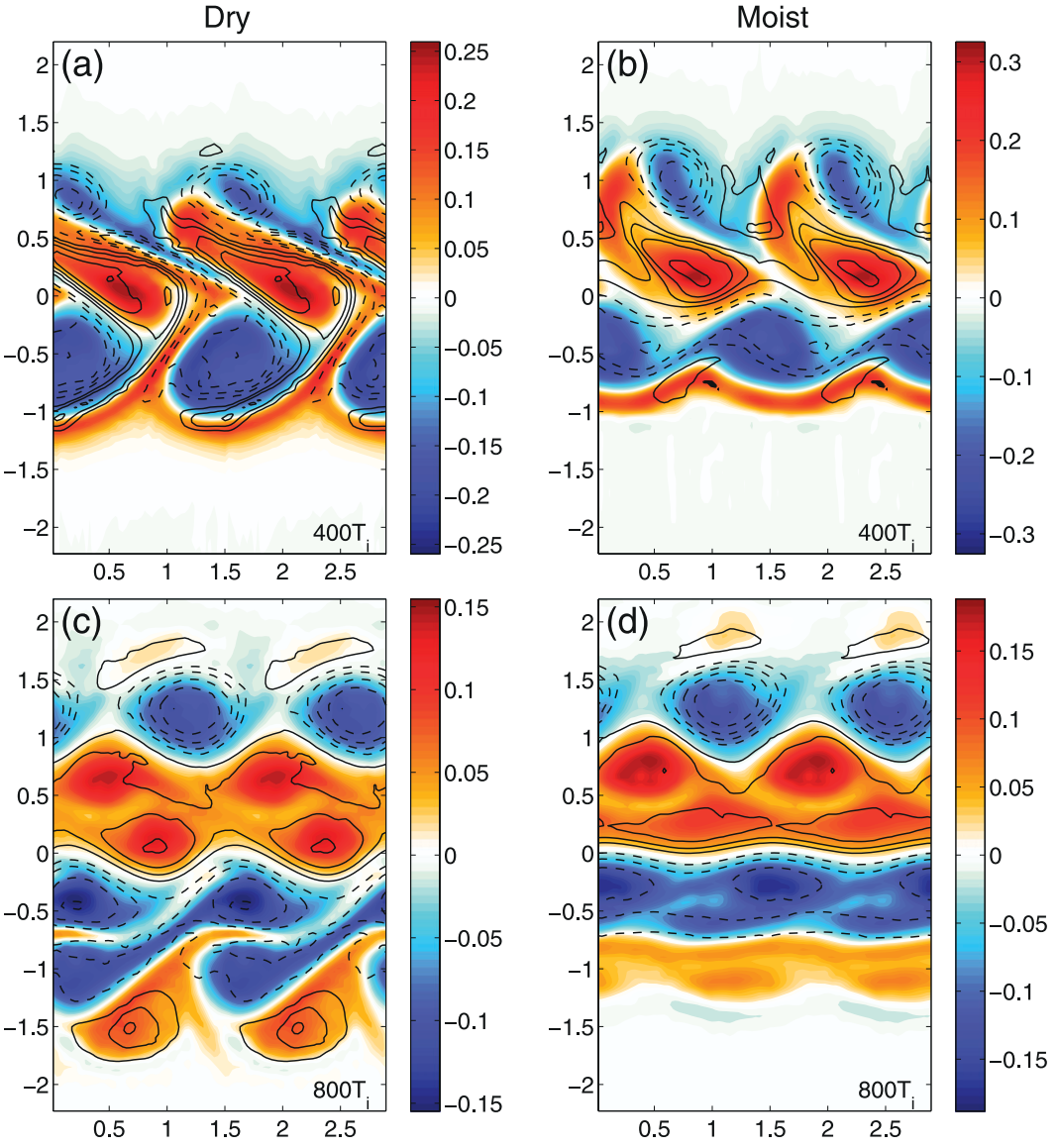

FIG. 13. As in Fig. 11, but for later times.

mc2RSW model, as was already emphasized. The quantification of the ageostrophic motions is important both from the conceptual point of view on the validity of the balanced models (Zeitlin 2008), in particular in the presence of condensation and latent heat release, and from the point of view of diagnosing vertical motions and IGW emissions. Let us remind that, although vertical velocity is absent in the equations of the RSW models, it is implicitly present and can be recovered via the divergence field.

In the 2RSW model, the divergence of the barotropic velocity field $\boldsymbol{v}^{\mathrm{bt}} = (h_1\boldsymbol{v}_1 + h_2\boldsymbol{v}_2)/(h_1 + h_2)$ is related to the ageostrophic motions of the free surface, whereas the divergence of the baroclinic velocity field $\boldsymbol{v}^{\mathrm{bc}} = \boldsymbol{v}_2 - \boldsymbol{v}_1$ is rather related to the motions of the interface between the two layers. For the vertical velocity across the layers, we have $w \propto \nabla \cdot \boldsymbol{v}^{\mathrm{bc}}$ if barotropic divergence is small, as is the case in our simulations. Unlike the free surface, the interface evolution is directly affected by the mass flux βP induced by condensation in the mc2RSW model.

Figure 16 shows the baroclinic divergence $\delta_{\mathrm{bc}} = \nabla \cdot \boldsymbol{v}^{\mathrm{bc}}$ in the dry and moist simulations. In the dry case, strong baroclinic divergence ($\delta_{\mathrm{bc}} > 0$) and convergence ($\delta_{\mathrm{bc}} < 0$) areas occur between lower-layer cyclones and anticyclones (see Figs. 16a,c). They correspond to strong ascent ($\delta_{\mathrm{bc}} > 0$) and descent ($\delta_{\mathrm{bc}} < 0$) air motions across the interface. During the nonlinear development of the instability ($t \geq 300T_i$), strong fronts form between these

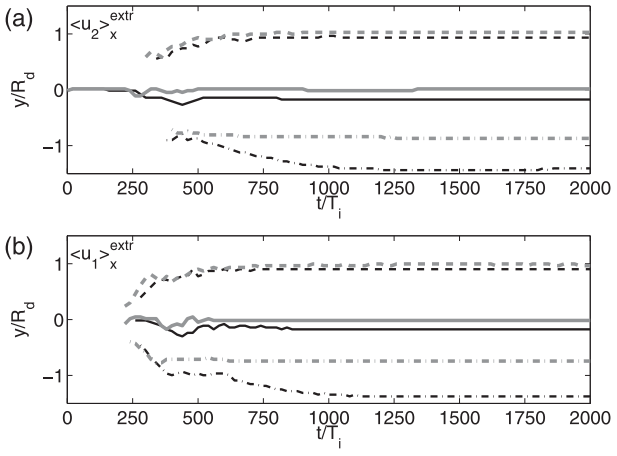

FIG. 14. Meridional positions of the first three extrema of the mean zonal jets $\langle u_i \rangle_x$ in (a) the upper and (b) the lower layer, for the dry (black lines) and moist (gray lines) simulations. The solid line is the main westerly jet, and the dotted–dashed (dashed) lines are southern (northern) easterly jets.

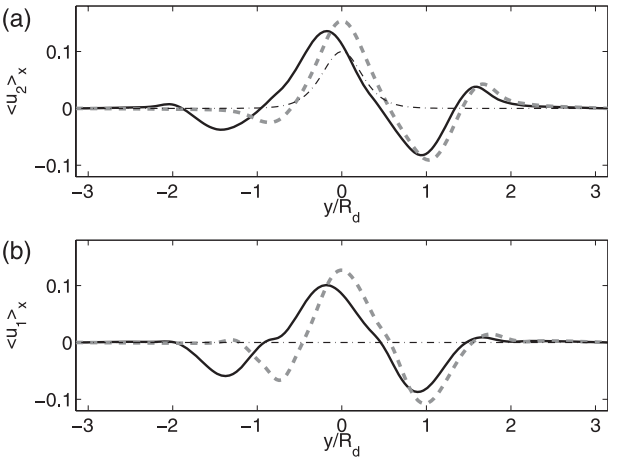

FIG. 15. Mean zonal velocity $\langle u_i \rangle_x$ in (a) the upper and (b) the lower layers at $t = 2000T_i$ for the dry (solid black lines) and moist (dashed gray lines) simulations as a function of y. The dotted–dashed lines mark the initial profile.

areas (see Figs. 16e,g). This is the classical path of air motions for the baroclinic instability: dry cold air descends (southeastward) and pushes through the strong front lower moist, warm air, which rises (northward). In the moist simulations, precipitation is triggered in the convergence zones where moisture exceeds its saturation value Q^s (Fig. 16b). Once triggered, condensation significantly intensifies the vertical motions in return, especially the lower-layer convergence, since $P_{\tau \to 0} = -Q^s \nabla \cdot \boldsymbol{v}_1 > 0$ (Figs. 16d,f). As to the baroclinic divergence, one can see hints of IGW emission from each side of the jet in both simulations, but its amplitude is too weak to be visible in Fig. 16.

Ageostrophic barotropic motions remain weak in both simulations (Fig. 17). In the dry case, they present continuous emission of IGW from each side of the jet (see Fig. 17a at $t = 200T_i$). The structure of these motions is modified in a complex fashion during the nonlinear development of the instability at $t \geq 300T_i$ (Figs. 17e,g). In the moist case, the spatial structure is similar to the dry case at $t = 200T_i$ (cf. Figs. 17a,b), except that the amplitude is twice as large. Condensation locally increases the amplitude of IGW at all times, especially around the strong cyclone in the lower layer. The spatial distribution of the barotropic divergence organizes along the vorticity fronts, as can be inferred from Figs. 11f and 17f. This is less the case for the dry simulation (cf. Figs. 11e, 17e). The structure of IGW around the cyclone is reminiscent of the baroclinic wave breaking in the primitive equation models (e.g., Plougonven and Snyder 2007). Note that no appearance of the internal wave capture by the jet is observed, even in the dry simulation. This is due to the different dispersion relations of IGW in continuously stratified and layered models.

The intensity of the ageostrophic motions can be quantified using the ageostrophy norm defined by

$$s_\delta^2 = \frac{1}{2} \int\int [(\nabla \cdot \boldsymbol{v}_1)^2 + (\nabla \cdot \boldsymbol{v}_2)^2] \, dx \, dy. \qquad (6.4)$$

Figure 18a shows its evolution in the dry and moist simulations. This is to be compared to the total precipitation integrated over the domain $P_{\text{tot}} = \int\int P \, dx \, dy$ (Fig. 18b). In both simulations, ageostrophic motions are intense during the wave breaking and the equilibration of the flow at $200T_i < t < 800T_i$. In the moist simulation, the ageostrophy norm reaches a noticeably large maximum value, 4 times larger than the dry counterpart, and is strongly correlated with the time evolution of total precipitation. A weak secondary peak appears at $t = 450T_i$ in the moist case and corresponds to the precipitating region, which emerges at the front of the northward-ejected dipole. At saturation, ageostrophic motions disappear for both simulations because no more precipitation occurs and a new geostrophic state tends to establish.

7. Summary and discussion

In this paper, we have studied baroclinic instability in the mc2RSW model, which is an idealized two-layer model of large-scale atmospheric dynamics, including condensation and latent heat release effects. This model is the simplest baroclinic moist-convective model that has the advantages to keep the dynamics related to ageostrophic motions and to be fully nonlinear. Contrary

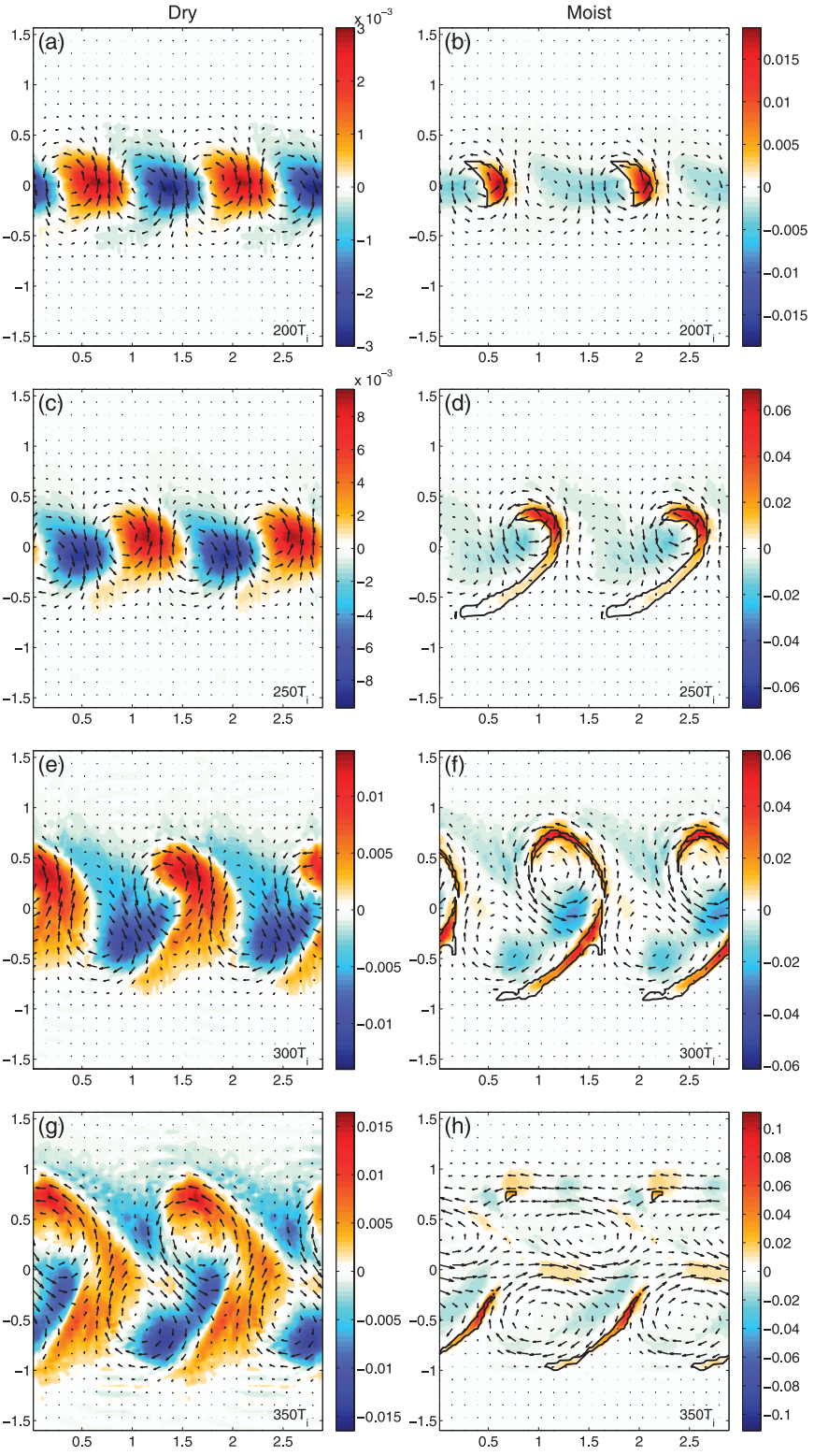

FIG. 16. Baroclinic divergence field $\delta_{bc} = \nabla \cdot \boldsymbol{v}^{bc}$ for the (a),(c),(e),(g) dry and (b),(d),(f),(h) moist simulations. Times (a),(b) $t = 200T_i$; (c),(d) $t = 250T_i$; (e),(f) $t = 300T_i$; and (g),(h) $t = 350T_i$. Lower-layer velocity field $\boldsymbol{v}_1$ is represented by arrows, and precipitating region is delimited by the thick black contour. Note that the color scale changes from panel to panel.

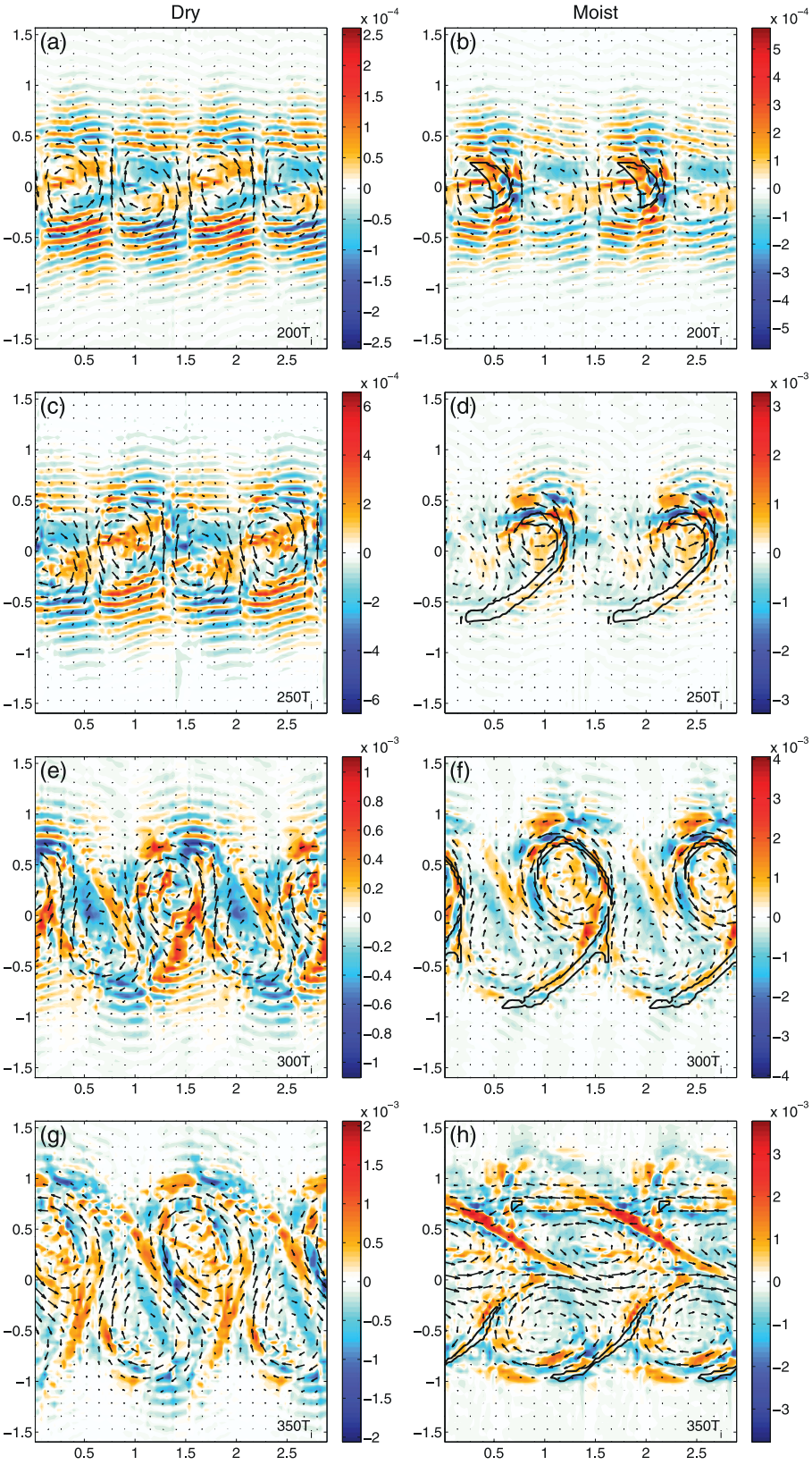

FIG. 17. As in Fig. 16, but for the barotropic divergence field $\delta_{bt} = \nabla \cdot \boldsymbol{v}^{bt}$.

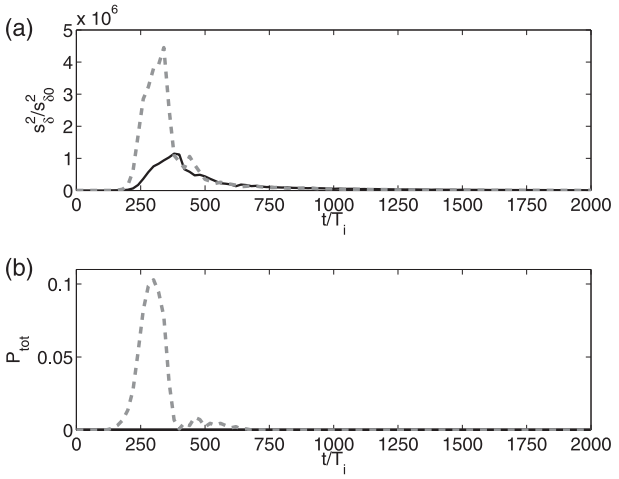

FIG. 18. (a) Divergence norm s_δ^2 of the perturbation and (b) total precipitation P_{tot} for the dry (solid black lines) and moist (dashed gray line) simulations, as a function of time.

to most of the models previously used to study the moist baroclinic instability (e.g., Emanuel et al. 1987; Balasubramanian and Yau 1994), it contains the evolution of the bulk humidity in the lower layer Q, an ''active'' tracer that triggers precipitation once the saturation threshold is exceeded. The model allows for cheap and efficient high-resolution numerical simulations with a new-generation finite-volume code (Bouchut and Zeitlin 2010).

We performed a thorough linear stability analysis of a balanced baroclinic Bickley jet in subsaturated conditions ($P \equiv 0$). The instability was found to be mainly baroclinic, extracting potential energy from the baroclinic Bickley jet. The identified most unstable baroclinic mode was used to initialize direct numerical simulations of the evolution of the baroclinic instability in dry (precipitation switched off) and moist (precipitation switched on once saturation threshold in moisture is reached, no sources of moisture) regimes.

The dry simulation correctly reproduces the classical cyclonic wave-breaking (LC2/CWB) life cycle of the baroclinic instability. We show that it leads to formation of a main vortex street at the initial jet axis and of two secondary ones (easterly jets) by ejection of asymmetric vortex dipoles. In the moist simulation, the onset of precipitation suddenly and significantly increases the growth rate of the instability at the initial stages. This is essentially due to the production of available potential energy through the latent heat release. Moisture anomalies are phase locked with lower-layer vorticity during the initial stage. Compared to the dry case, the evolution in the moist case is clearly accelerated. The precipitating regions appear as a comma along the outer side of the lower-layer cyclones, in agreement with observed synoptic situations. Condensation temporary but significantly intensifies the ageostrophic motions and the lower-layer cyclones. The condensation-induced cyclone–anticyclone asymmetry modifies the equilibration of the flow: no southward ejection of dipoles is observed and the vortex streets and the associated mean zonal jets at the equilibrium are shifted northward with respect to the dry case. We found only weak differences in the norms of the perturbation in dry and moist simulations at the very end of the evolution.

It should be emphasized that our simple model gives very plausible results on nonlinear saturation of the instability both in dry and precipitating cases, which makes us think that the model is a good compromise between simplicity and representativeness of the essential physical phenomena. In this connection, let us remind that in the present study we limited ourselves by a simplest configuration with uniform initial humidity and no evaporation. Both restrictions can be easily relaxed.

Our study may be compared with the studies of the role of water vapor on storm tracks and baroclinic eddies. First, we confirm the temporal enhancement of the growth rate of the instability due to the condensation that was found by other idealized studies (e.g., Emanuel et al. 1987) or case studies (e.g., Wernli et al. 2002; Moore et al. 2008). Despite this enhancement, we observed that the perturbation energy (diagnosed with different norms) is almost the same after nonlinear saturation of the instability. This differs from our previous work (Lambaerts et al. 2011a) on moist barotropic instability [we remind the reader that the mcRSW model used in Lambaerts et al. (2011a) is a limit of infinitely thick upper layer of mc2RSW model]. The minor change in perturbation energy is reminiscent of the work of Bengtsson et al. (2009), who found in a warmer climate relative minor change in extratropical cyclones intensity (recall that a warmer climate is associated with a moister atmosphere). It can be mentioned that other studies obtained, on the other hand, a decrease of the eddy energy when increasing water vapor in the atmosphere (Laîné et al. 2011; Frierson et al. 2006) or for a warmer climate (O'Gorman 2010). Yet, our model is idealized and does not take into account other processes or forcing (no statistical equilibrium is reached) and thus cannot fully address this issue.

In our simulation, we confirm the northward shift of the zonal jet that was found in Laîné et al. (2011) and Frierson et al. (2006) when comparing dry and moist atmospheres. It is speculated that moisture could in fact be responsible of the meridional shift of the jet stream obtained in climate change scenarios (Yin 2005). The acceleration of the mean flow at the jet center we detected during the saturation of the instability for the

moist simulation does not confirm the results of Laîné et al. (2011) and Frierson et al. (2006), where a deceleration of the main upper-level jet was observed. We hypothesize that the intensification we observe is essentially due to the modification of the secondary instabilities, which change the LC2/CWB scenario in our simulations and could be a transient effect of our free-decay setting.

Acknowledgments. We are grateful to F. Bouchut for helpful discussions of the numerical aspects of this study. This work was supported by the French ANR Contract "SVEMO." GL acknowledges the support of the MAIF foundation through the Grant REVAE.

APPENDIX A

Some Details of the Linear Stability Analysis

The dimensionless Eqs. (2.1)–(2.3) linearized about the Bickley jet [Eqs. (3.2)–(3.3)] with $P \equiv 0$ and Fourier transformation lead to the following eigenproblem:

$$(\mathcal{L} - c\mathcal{I}) \begin{pmatrix} \hat{u}_1 \\ \hat{v}_1/ik \\ \hat{\eta}_1 \\ \hat{u}_2 \\ \hat{v}_2/ik \\ \hat{\eta}_2 \end{pmatrix} = 0, \tag{A.1}$$

where $c = \omega/k$ is the eigenvalue and $\mathcal{I}$ the 6×6 identity matrix. The 6×6 matrix $\mathcal{L}$ is defined by

$$\mathcal{L} = \begin{pmatrix} \mathcal{A} & \mathcal{B} \\ \mathcal{C} & \mathcal{D} \end{pmatrix}, \tag{A.2}$$

where

$$\mathcal{A} = \begin{bmatrix} 0 & -\dfrac{1}{\mathrm{Ro}} & \dfrac{1}{\mathrm{Ro}} \\ \dfrac{-1}{\mathrm{Ro}k^2} & 0 & \dfrac{-1}{\mathrm{Ro}k^2}\partial_y \\ \overline{\eta}_1 + \dfrac{\mathrm{Bu}D_1}{\mathrm{Ro}} & \partial_y\overline{\eta}_1 + \left(\overline{\eta}_1 + \dfrac{\mathrm{Bu}D_1}{\mathrm{Ro}}\right)\partial_y & 0 \end{bmatrix}, \tag{A.3}$$

$$\mathcal{B} = \begin{pmatrix} 0 & 0 & \dfrac{1}{\mathrm{Ro}} \\ 0 & 0 & \dfrac{-1}{\mathrm{Ro}k^2}\partial_y \\ 0 & 0 & 0 \end{pmatrix}, \tag{A.4}$$

$$\mathcal{C} = \begin{bmatrix} \overline{u}_2 & \partial_y\overline{u}_2 - \dfrac{1}{\mathrm{Ro}} & \dfrac{1}{\mathrm{Ro}} \\ \dfrac{-1}{\mathrm{Ro}k^2} & \overline{u}_2 & \dfrac{-\alpha}{\mathrm{Ro}k^2}\partial_y \\ \overline{\eta}_2 + \dfrac{\mathrm{Bu}D_2}{\mathrm{Ro}} & \partial_y\overline{\eta}_2 + \left(\overline{\eta}_2 + \dfrac{\mathrm{Bu}D_2}{\mathrm{Ro}}\right)\partial_y & \overline{u}_2 \end{bmatrix}, \tag{A.5}$$

and

$$\mathcal{D} = \begin{pmatrix} 0 & 0 & \dfrac{1}{\mathrm{Ro}} \\ 0 & 0 & \dfrac{-1}{\mathrm{Ro}k^2}\partial_y \\ 0 & 0 & 0 \end{pmatrix}. \tag{A.6}$$

This eigenproblem is solved by the collocation method (Trefethen 2000) in MATLAB with a high number of Chebychev points $N = 300$ for a y-domain length $L_y = 20L$. A difficulty of the method is the appearance of pseudomodes with critical latitudes $y = y_c$ defined by $\overline{u}_2(y_c) = c_p$ inside the jet. They are filtered by a test on the convergence of the eigenvalues for $\Delta N = +10$ and the gradient limiter method (Scherer and Zeitlin 2008).

APPENDIX B

Initial Readjustment Process

The initial geostrophic readjustment that we observed in our simulations is essentially caused by numerical discretization errors. This does not contradict the well-balanced character of the scheme. In fact, the latter property means that the scheme preserves the balanced state (in the numerical sense) and that small errors do not grow for a stable state. The readjustment does not disappear with higher spatial resolution and occurs even if no perturbation is superimposed on the initial jet. Nevertheless, readjustment does not significantly modify the main evolution of the instability because the amplitudes of the emitted IGW are weak (baroclinic waves: $\sim 10^{-4}$ and barotropic waves: $\sim 10^{-5}$), and the new geostrophic state to which the system tends is very close to the initial one.

Figure B1 shows the Hovmöller diagram of the baroclinic and the barotropic divergence fields at $x = 0.7R_d$ for early times. The propagation of slow internal (mostly baroclinic) and rapid external (mostly barotropic) IGW is seen. Their respective higher velocities correspond well to the (dry) linear internal c_i and external c_e characteristic velocities that are found in Lambaerts et al. (2011b), $c_i = 0.15\sqrt{gH_0}$ and $c_e = 1.01\sqrt{gH_0}$. Waves are emitted to the northern and southern boundaries, which dissipate and partially reflect them.

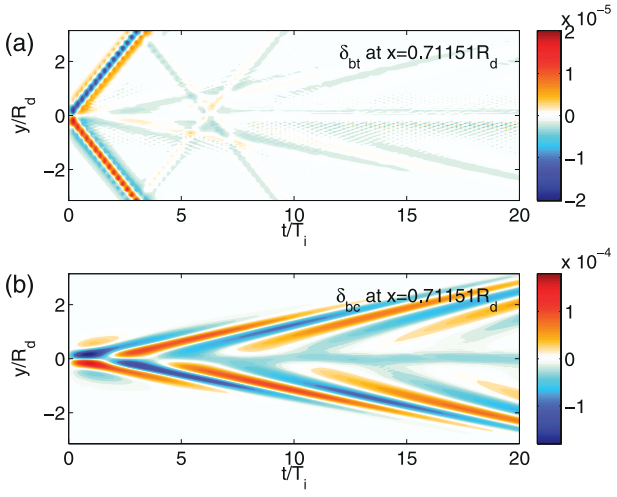

FIG. B1. Hovmöller diagrams of (a) the barotropic and (b) the baroclinic divergence fields at the early stage of the simulations.

APPENDIX C

Dependence of the Results on the Parameters

The simulations presented above are sensitive to the values of parameters, in particular related to moisture: the initial value of the uniform moisture field Q_0 and the parameter β, which is linked to the latent heat coefficient (see Lambaerts et al. 2011b).

The gap $Q^s - Q_0$ was chosen to trigger precipitation at $t = 100T_i$ when the dry perturbation exponentially grows. For smaller value of Q_0, precipitation could occur at the end of (or after) the exponential growth of the perturbation. In this case, the condensation effects are reduced. Obviously, if Q_0 is too small, the maximum of the moisture field never reaches the saturation Q^s and the moist simulation becomes identical to the dry one.

The coefficient β controls the intensity of the mass flux βP. Because the mean specific humidity of an air parcel Q/h_1 always decreases in precipitating regions,

$$(\partial_t + \boldsymbol{v}_1 \cdot \nabla)\frac{Q}{h_1} = -\left(1 - \frac{\beta Q}{h_1}\right)\frac{\beta P}{h_1} < 0, \quad \text{(C.1)}$$

for positive moist enthalpy $m_1 = h_1 - \beta Q > 0$, the coefficient β must satisfy

$$0 < \beta < \frac{\min\{h_1(x, y, 0)\}}{Q_0} = \beta_\star. \quad \text{(C.2)}$$

For the moist simulation, the upper limit is given by $\beta_\star \sim 1.06$.

Figure C1a shows the evolution of the maximum of the exponential growth rate $\sigma^{\max}$ as a function of β. As

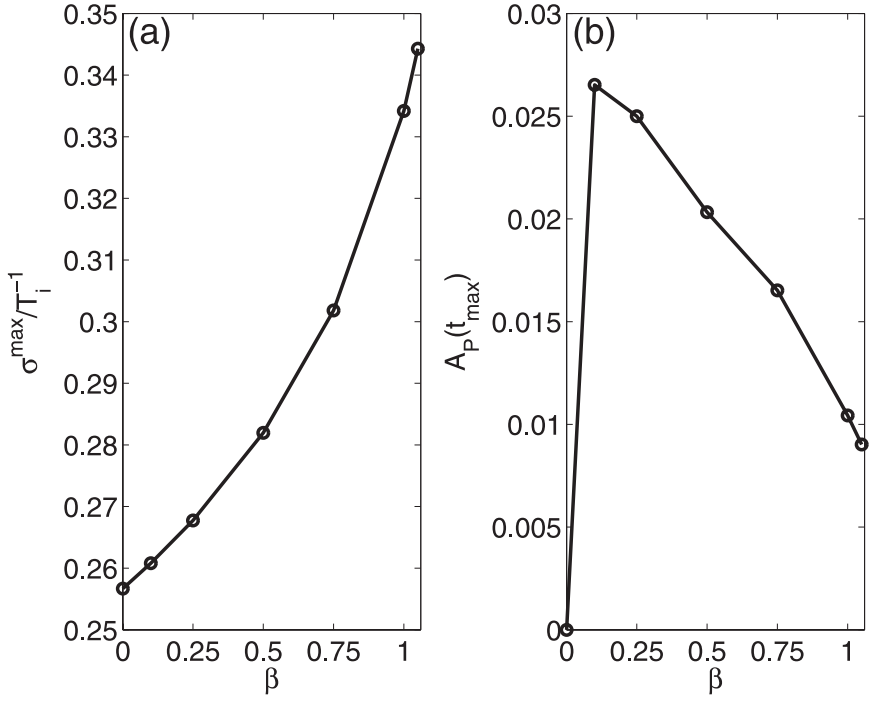

FIG. C1. (a) Maximum of the exponential growth rate $\sigma^{\max}$ and (b) the corresponding fraction of the area occupied by precipitation A_P as functions of the parameter β.

expected, it is an increasing function of β because condensation becomes more efficient. Note that this function does not seem to diverge when β approaches $\beta_\star$ because this latter does not correspond to the loss of hyperbolicity for the mc2RSW model due to precipitation, as was the case in the one-layer model (Lambaerts et al. 2011a). One can show that the hyperbolicity loss at increasing β (>1.5) is here essentially caused by the strong lower-layer relative vorticity and the related vertical shear.

The fraction of the area occupied by precipitation A_P at the time at which the growth rate reaches its maximum value is shown in Fig. C1b as a function of β. This fraction decreases when the impact of the latent heat release increases, in agreement with previous studies (Emanuel et al. 1987; Lapeyre and Held 2004).

REFERENCES

Arakawa, A., and W. H. Schubert, 1974: Interaction of a cumulus cloud ensemble with the large-scale environment, part I. *J. Atmos. Sci.,* **31,** 674–701.

Balasubramanian, G., and M. K. Yau, 1994: Baroclinic instability in a two-layer model with parameterized slantwise convection. *J. Atmos. Sci.,* **51,** 971–990.

——, and ——, 1996: The life cycle of a simulated marine cyclone: Energetics and PV diagnostics. *J. Atmos. Sci.,* **53,** 639–653.

——, and S. T. Garner, 1997: The equilibration of short baroclinic waves. *J. Atmos. Sci.,* **54,** 2850–2871.

Bannon, P. R., 1986: Linear development of quasi-geostrophic baroclinic disturbances with condensational heating. *J. Atmos. Sci.,* **43,** 2261–2276.

Bengtsson, L., K. I. Hodges, and N. Keenlyside, 2009: Will extratropical storms intensify in a warmer climate? *J. Climate,* **22,** 2276–2301.

Betts, A. K., and M. J. Miller, 1986: A new convective adjustement scheme. Part II: Single columns tests using GATE wave, BOMEX, ATEX and arctic air-mass data sets. *Quart. J. Roy. Meteor. Soc.,* **112,** 693–709.

Bluestein, H. B., 1993: *Observations and Theory of Weather Systems*. Vol. 2, *Synoptic-Dynamic Meteorology in Midlatitudes,* Oxford University Press, 608 pp.

Bouchut, F., and V. Zeitlin, 2010: A robust well-balanced scheme for multi-layer shallow water equations. *Discrete Cont. Dyn. Syst.,* **13B,** 739–758.

——, J. Lambaerts, G. Lapeyre, and V. Zeitlin, 2009: Fronts and nonlinear waves in a simplified shallow-water model of the atmosphere with moisture and convection. *Phys. Fluids,* **21,** 116604, doi:10.1063/1.3265970.

Browning, K. A., 1986: Conceptual models of precipitation systems. *Wea. Forecasting,* **1,** 23–41.

Cairns, R. A., 1979: The role of negative energy waves in some instabilities of parallel flows. *J. Fluid Mech.,* **92,** 1–14.

Charney, J. G., 1947: The dynamics of the long waves in a baroclinic westerly current. *J. Meteor.,* **4,** 135–165.

——, and A. Eliassen, 1964: On the growth of the hurricane depression. *J. Atmos. Sci.,* **21,** 68–75.

Davies, H. C., Ch. Schär, and H. Wernli, 1991: The palette of fronts and cyclones within a baroclinic wave development. *J. Atmos. Sci.,* **48,** 1666–1689.

Eady, E. T., 1949: Long waves and cyclone waves. *Tellus,* **1,** 33–52.

Emanuel, K. A., 1994: *Atmospheric Convection*. Oxford University Press, 580 pp.

——, M. Fantini, and A. J. Thorpe, 1987: Baroclinic instability in an environment of small stability to slantwise moist convection. Part I: Two-dimensional models. *J. Atmos. Sci.,* **44,** 1559–1573.

——, J. D. Neelin, and C. S. Bretherton, 1994: On large-scale circulations in convecting atmospheres. *Quart. J. Roy. Meteor. Soc.,* **120,** 1111–1143.

Frierson, D. M. W., A. J. Majda, and O. M. Pauluis, 2004: Large scale dynamics of precipitation fronts in the tropical atmosphere: A novel relaxation limit. *Commun. Math. Sci.,* **2,** 591–626.

——, I. M. Held, O. Pauluis, and P. Zurita-Gotor, 2006: A gray-radiation aquaplanet moist GCM. Part I: Static stability and eddy scale. *J. Atmos. Sci.,* **63,** 2548–2566.

Gill, A. E., 1982: Studies of moisture effects in simple atmospheric models: The stable case. *Geophys. Astrophys. Fluid Dyn.,* **19,** 119–152.

Gutowski, W. J., L. E. Branscome, and D. A. Stewart, 1992: Life cycles of moist baroclinic eddies. *J. Atmos. Sci.,* **49,** 306–319.

Hazel, P., 1972: Numerical studies of the stability of inviscid stratified shear flows. *J. Fluid Mech.,* **51,** 39–61.

Heifetz, E., C. H. Bishop, B. J. Hoskins, and J. Methven, 2004: The counter-propagating Rossby-wave perspective on baroclinic instability. I: Mathematical basis. *Quart. J. Roy. Meteor. Soc.,* **130,** 211–231.

Holton, J. R., 1972: *An Introduction to Dynamic Meteorology*. Academic Press, 319 pp.

Hoskins, B. J., and F. P. Bretherton, 1972: Atmospheric frontogenesis models: Mathematical formulation and solution. *J. Atmos. Sci.,* **29,** 11–37.

——, and N. G. West, 1979: Baroclinic waves and frontogenesis. Part II: Uniform potential vorticity jet flows-cold and warm fronts. *J. Atmos. Sci.,* **36,** 1663–1680.

——, M. E. McIntyre, and A. W. Robertson, 1985: On the use and significance of isentropic potential vorticity maps. *Quart. J. Roy. Meteor. Soc.,* **111,** 877–946.

Laîné, A., G. Lapeyre, and G. Rivière, 2011: A quasigeostrophic model for moist storm tracks. *J. Atmos. Sci.,* **68,** 1306–1322.

Lambaerts, J., G. Lapeyre, and V. Zeitlin, 2011a: Moist versus dry barotropic instability in a shallow-water model of the atmosphere with moist convection. *J. Atmos. Sci.,* **68,** 1234–1252.

——, ——, ——, and F. Bouchut, 2011b: Simplified two-layer models of precipitating atmosphere and their properties. *Phys. Fluids,* **23,** 046603, doi:10.1063/1.3582356.

Lapeyre, G., and I. M. Held, 2004: The role of moisture in the dynamics and energetics of turbulent baroclinic eddies. *J. Atmos. Sci.,* **61,** 1693–1710.

Lindzen, R. S., 1974: Wave-CISK in the tropics. *J. Atmos. Sci.,* **31,** 156–179.

Lorenz, E. N., 1955: Available potential energy and the maintenance of the general circulation. *Tellus,* **7,** 157–167.

Mak, M., 1982: On moist quasi-geostrophic baroclinic instability. *J. Atmos. Sci.,* **39,** 2028–2037.

Moore, R. W., M. T. Montgomery, and H. C. Davies, 2008: The integral role of a diabatic Rossby vortex in a heavy snowfall event. *Mon. Wea. Rev.,* **136,** 1878–1897.

O'Gorman, P. A., 2010: Understanding the varied response of the extratropical storm tracks to climate change. *Proc. Nat. Acad. Sci. USA,* **107,** 19 176–19 180.

——, 2011: The effective static stability experienced by eddies in a moist atmosphere. *J. Atmos. Sci.,* **68,** 75–90.

Pedlosky, J., 1979: *Geophysical Fluid Dynamics*. Springer-Verlag, 624 pp.

Phillips, N. A., 1954: Energy transformations and meridional circulations associated with simple baroclinic waves in a two-level, quasi-geostrophic model. *Tellus,* **6,** 273–286.

Plougonven, R., and C. Snyder, 2007: Inertia–gravity waves spontaneously generated by jets and fronts. Part I: Different baroclinic life cycles. *J. Atmos. Sci.,* **64,** 2502–2520.

Sakai, S., 1989: Rossby-Kelvin instability: A new type of ageostrophic instability caused by resonance between Rossby waves and gravity waves. *J. Fluid Mech.,* **202,** 149–176.

Schecter, D. A., 2011: Evaluation of a reduced model for investigating hurricane formation from turbulence. *Quart. J. Roy. Meteor. Soc.,* **137,** 155–178.

——, and T. J. Dunkerton, 2009: Hurricane formation in diabatic Ekman turbulence. *Quart. J. Roy. Meteor. Soc.,* **135,** 823–838.

Scherer, E., and V. Zeitlin, 2008: Instability of coupled geostrophic density fronts and its nonlinear evolution. *J. Fluid Mech.,* **613,** 309–327.

Shukla, J., 1978: CISK-barotropic-baroclinic instability and the growth of monsoon depressions. *J. Atmos. Sci.,* **35,** 495–508.

Thorncroft, C. D., B. J. Hoskins, and M. E. McIntyre, 1993: Two paradigms of baroclinic-wave life-cycle behavior. *Quart. J. Roy. Meteor. Soc.,* **119,** 17–55.

Trefethen, L. N., 2000: *Spectral Methods in MATLAB*. SIAM, 165 pp.

Wernli, H., S. Dirren, M. A. Liniger, and M. Zillig, 2002: Dynamical aspects of the life cycle of the winter storm 'Lothar.' *Quart. J. Roy. Meteor. Soc.,* **128,** 405–429.

Whitaker, J. S., and C. A. Davis, 1994: Cyclogenesis in a saturated environment. *J. Atmos. Sci.,* **51,** 889–908.

Yin, J. H., 2005: A consistent poleward shift of the storm tracks in simulations of 21st century climate. *Geophys. Res. Lett.,* **32,** L18701, doi:10.1029/2005GL023684.

Zeitlin, V., 2008: Decoupling of balanced and unbalanced motions and inertia–gravity wave emission: Small versus large Rossby numbers. *J. Atmos. Sci.,* **65,** 3528–3542.